Ultrastructural diversity of alpha-Synuclein pathology in the post-mortem brain of Parkinson patients: implications for Lewy Body formation

Amanda J Lewis[1,2#], Lukas van den Heuvel[1,2], Marta di Fabrizio[1,2], Domenic Burger[1,2], Evelien Huisman[3], John GJM Bol[3], Wilma DJ van de Berg[3,4], Henning Stahlberg[1,2].

1. Laboratory of Biological Electron Microscopy, School of Basic Sciences, Federal Institute of Technology Lausanne (EPFL), Lausanne, Switzerland.

2. Department of Fundamental Microbiology, University of Lausanne, Lausanne Switzerland

3. Department of Anatomy and Neurosciences, section Clinical Neuroanatomy and Biobanking, Amsterdam Neuroscience, Amsterdam University Medical Centre, Vrije University Amsterdam, 1081 HZ, Amsterdam, The Netherlands.

4. Amsterdam Neuroscience program Neurodegeneration, Amsterdam University Medical Centre, Vrije University Amsterdam, 1081 HZ, Amsterdam, The Netherlands

correspondence to: amanda.lewis@epfl.ch

Abstract

Lewy bodies, the major pathological hallmark of Parkinson's disease, are intraneuronal inclusions rich in aggregated alpha-synuclein (aSyn). To understand the cellular mechanisms behind the formation of Lewy bodies and the aggregation of aSyn, we used correlative light and electron microscopy and detailed ultrastructural analysis of postmortem brain tissue samples of Parkinson patients. We found that somal aSyn inclusions in dopaminergic neurons were exclusively fibrillar, while membranous-type inclusions were located outside the cell soma and likely compact neuritic aggregates. These neuritic inclusions displayed phenotypic heterogeneity, ranging from predominantly membranous to mixed membranous/fibrillar ultrastructures. Our data suggest that membranous and fibrillar aSyn inclusions form via distinct mechanisms, with membranous neuritic inclusions providing the environment for the initial nucleation of aSyn fibrils, which could then spread via a prion-like mechanism to form somal fibrillar Lewy bodies. This study provides important insight into Lewy body formation and highlights the importance of aSyn and membrane interactions for future therapeutic intervention.

Introduction

Lewy bodies (LBs) are abnormal intracellular inclusions rich in aggregated alpha-synuclein (aSyn). First identified in the *substantia nigra*, where defects in the dopaminergic neurons lead to the characteristic motor function failures in PD patients[1], they now represent the major pathological hallmark of Parkinson's disease (PD) and Dementia with Lewy bodies (DLB). Classic histopathological staining of post-mortem brain tissue initially revealed LBs as spherical structures with a dense core and a pale halo[2] that was immuno-positive for aSyn[3]. Later, transmission electron microscopy (EM) attributed the core to a region of highly electron-dense material, and the halo to aSyn-fibrils radiating outwards[4–7].

Experiments in cellular and animal PD models demonstrate that aSyn fibrils can be taken up by neurons[8–11], and that the fibrils can spread from one cell to another[8,12,13], suggesting a possible mechanism for the gradual spreading of LBs through the brain in a caudal-to-rostral manner[14]. *De novo* formation of aSyn fibrils likely involves (1) protein misfolding, (2) clustering of misfolded protein into oligomers, and (3) aggregation of oligomers into long fibrils[15,16]. Throughout this process, several post-translational modifications including phosphorylation, ubiquitination and truncation of the C-terminus are believed to modulate aSyn misfolding and LB formation[17]. In particular, the finding that aSyn in LBs is extensively phosphorylated at the serine residue 129 ($aSyn^{pS129}$)[18] paved the way for its use as a key biochemical and histological marker for synucleinopathies. Generally, aSyn misfolding and fibril formation have been a major focus of scientific PD research in the past 30 years.

However, the components comprising LBs include numerous other elements including lipids[19,20], organelles[5], membranous fragments[21], and more than 100 additional proteins[7,22]. Moreover, not only is the biochemical composition of LBs extremely heterogeneous, but also their histological and ultrastructural morphologies. Other types of brainstem Lewy pathology, namely Lewy neurites, bulgy neurites and pale bodies, have also been reported to contain aSyn fibrils as a major component but exhibit different morphologies compared to the classic halo LBs. Lewy neurites are rod-shaped inclusions in neuronal projections[14], and pale bodies are large aggregates in neuronal cytoplasm, which are weakly stained by hematoxylin & eosin[23], often irregular in shape and with an ultrastructure consisting of randomly organized fibrils intermixed with clusters of mitochondria and other organelles[23–25]. Additionally, our recent study using correlative light and electron microscopy (CLEM) characterized other forms of Lewy pathology enriched in lipids and membranous structures[21]. These structures, here referred to as membranous pathology, are ultrastructurally distinct from fibrillar inclusions by their high proportion of vesicles and membrane fragments co-localizing with aSyn phosphorylated at Serine 129 ($aSyn^{pS129}$) immunoreactivity in the absence of any observable fibrils by EM.

Several studies have proposed a process for the formation of LBs, based on the different morphologies of aSyn immuno-staining in combination with disease staging[14,26–29]. This proposed process includes the accumulation of diffuse cytoplasmic staining or punctate dots, followed by the development of a small aggregation center that grows into a pale body and

finally develops into the classic fibrillar halo LB. Pale bodies are considered precursors to fibrillar LBs. Pale bodies are more abundant in the early stages of PD compared to halo LBs, and several pale bodies often co-exist in the same cell[23,30]. The appearance of Lewy neurites is thought to precede the appearance of somal aSyn pathology[14], however it is unclear how Lewy neurites specifically relate to the development of the LBs. Further, it is not known how the membranous pathology fits into the proposed timeline for LB formation. As there are currently no animal or cellular models that can reproduce the large diversity of human PD pathology, to infer a mechanism for LB formation requires studying their morphological heterogeneity in the human post-mortem brain.

In this study, we have used CLEM to investigate aSyn inclusions in the *substantia nigra* of post-mortem PD brain donors, targeting morphologies that form the proposed timeline of LB formation. We found that the aSyn pathology in the *substantia nigra* can be classified based on distinct ultrastructural characteristics, depending upon whether it occurs in the soma of neuromelanin containing neurons or not. The inclusions found in neuromelanin containing neurons consistently exhibited fibrillar ultrastructures. The increasing density of accumulated fibrils matches the proposed timeline for LB formation culminating in three distinct stages of fibril organization for halo LBs. Notably, all membranous inclusions observed were not located within the cell soma and displayed a variety of ultrastructures including membranous only (with an absence of fibrils), membranes intermixed with fibrils, and a halo of membranes surrounding a fibrillar core. We present an example where all these ultrastructures are present within the same neuritic inclusion suggesting that membranous inclusions could provide the environment for the formation of aSyn fibrils and may represent the initial stages of aSyn aggregation. Finally, we hypothesize that aSyn aggregates together with membranes, seeding the nucleation of aSyn fibrils which then accumulate and spread via a prion-like mechanism to eventually form the mature halo-LB in the soma of dopaminergic neurons.

Results

Localisation of aSyn pathology using CLEM

To localize aSyn pathology in post-mortem human brain, we used CLEM as described previously[31] on free-floating 40-60 µm semi-thin sections immuno-labeled against aSyn^{pS129} and detected pathology pre-embedding using fluorescence microscopy (CLEM^{FL}) or post-embedding using immunohistochemistry (IHC; CLEM^{IHC}). In the free-floating sections, we targeted pathology in neuromelanin containing neurons showing various staining patterns by immuno-fluorescence, including diffuse/punctate cellular aSyn^{pS129}, small and large aggregates, and large aggregates with a distinct aSyn^{pS129} halo (halo LBs), and large aggregates with halo LBs at the periphery. A neurofilament marker (against neurofilament heavy chain) and DAPI staining for cell nuclei were used to help delineate the cellular context for the inclusions where neuromelanin was absent (Figure 1a-d). Large aggregates that were not clearly within a cell soma (due to lack of neuromelanin and cellular markers) and bulgy Lewy

neurites were also included for investigation with EM (Figure 1e,f). We often observed a ring of neurofilament staining on the inside of intracellular aSyn^{pS129} halo LBs, as previously reported by Moors et al.[29] (Figure 1d). We also often observed a ring of neurofilament immuno-fluorescence surrounding the non-somal aSyn^{pS129} inclusions, indicating that these inclusions were of neuronal origin. As these inclusions had similar dimensions in the x,y and z planes they are likely to be compact neuritic (axonal, dendritic, or synaptic) aggregates, rather than cross-sections through elongated bulgy Lewy neurites (Figure 1f).

Using this CLEM pipeline, we characterized 92 aSyn immuno-positive inclusions (Supplementary Table 1) from within the *substantia nigra* of ten brain donors (Supplementary Table 2). In total, 30 representative inclusions are described in detail here.

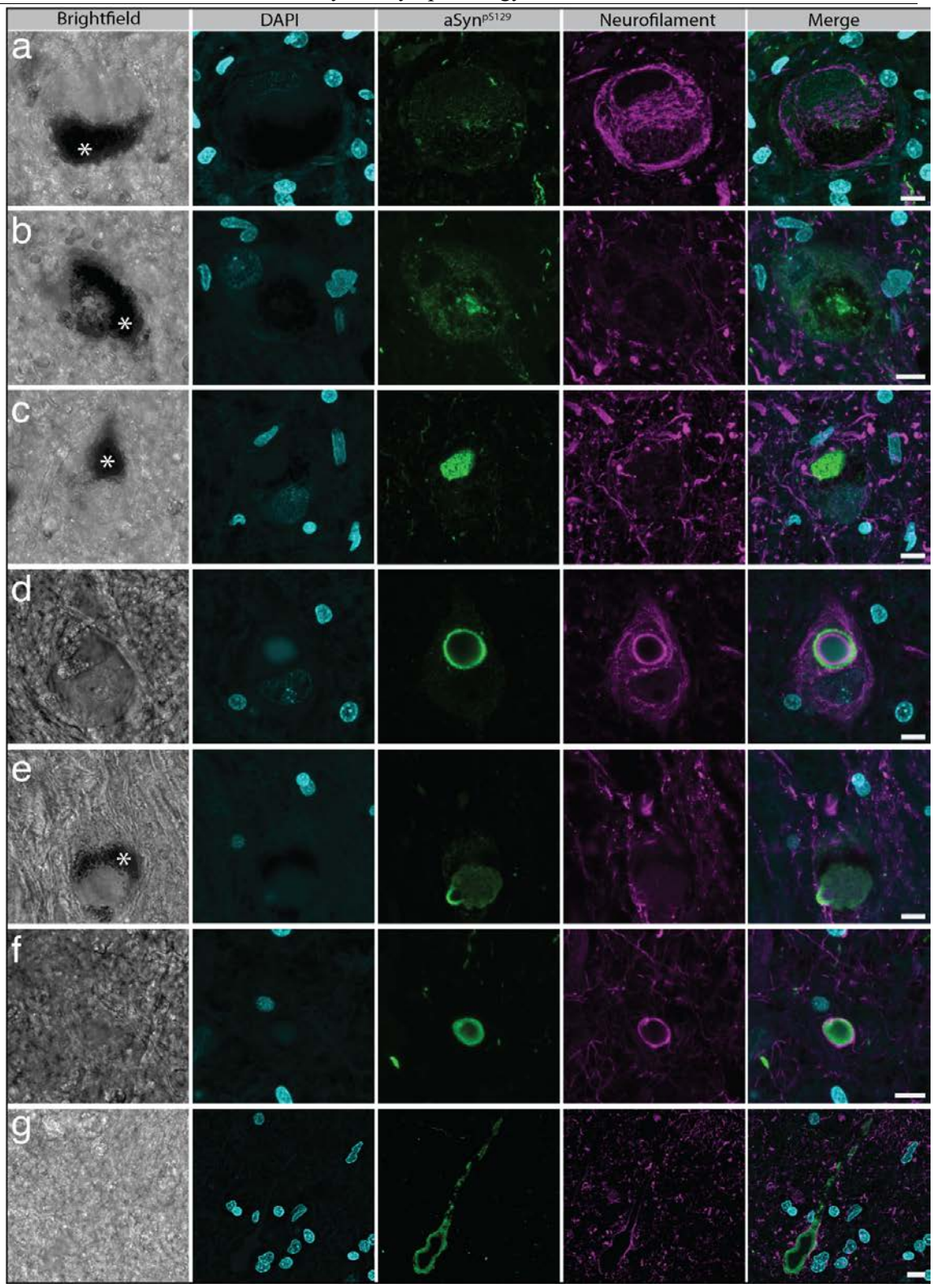

Figure 1. Morphological staining patterns of aSyn pathology targeted for EM. Maximum projection images of confocal z-stacks of **(a)** diffuse/punctate cellular staining (z = 13.8 µm), **(b)** small aggregates (z = 9 µm) **(c)** large aggregates (z = 9 µm) **(d)** halo LBs (z = 5.4 µm) **(e)** large aggregates with a halo LB at the periphery (z = 7.5 µm) **(f)** compact neuritic aggregates (z = 4.2 µm)and **(g)** Lewy/bulgy neurites (z = 6 µm). The panels in each row show the same field of view. For each panel the brightfield, nuclear staining (DAPI; cyan), aSyn^{pS129}(11a5, Prothena; green), neurofilament (neurofilament H, Abcam;

magenta) and a merge of the fluorescent channels are shown. The presence of neuromelanin, visible in the brightfield channel (white asterisk), and/or neurofilament and DAPI staining was used to identify somal inclusions (a-e). Scale bars: 10 µm.

aSyn pathology in the soma of neuromelanin containing cells is distinctly fibrillar.

We first characterized the ultrastructure of aSyn inclusions which were clearly inside the soma of neuromelanin containing neurons and found that the ultrastructures were exclusively fibrillar. Following the proposed timeline of LB formation, diffuse/punctate aSyn immunoreactivity was often seen interspersed amongst the neuromelanin granules within the neuron. Due to the sparsity of the fluorescent signal in single z-planes throughout the cell, exact correlation of the aSyn immunopositive region with a specific ultrastructure by EM was not possible.

Small aggregates. Small aggregation centers were also often localized amongst the neuromelanin granules, and the correlated ultrastructure showed sparse fibrils intermixed with vesicles and proteinaceous material (Figure 2a). Although it cannot be ruled out that these fibrils belong to the cytoskeleton or other filamentous material, they are likely to be aSyn fibrils since their location corresponds to where the aSyn^{pS129} immuno-fluorescence is brightest. Mitochondria and components of the autophagy-lysosomal pathway were observed around the periphery of the aggregates, and sometimes clustered together amongst the fibrils (Figure 2a). The mitochondria close to the aggregates, and further out in the cytoplasm, were often swollen (> 1µm in diameter) and had fragmented cristae, and we also observed a mitophagy event near an aggregate (see figure 2a). Such dysfunctional mitochondrial phenotypes have been previously associated with PD[32,33].

Large aggregates or pale bodies. Large inclusions showing diffuse aSyn^{pS129} immuno-fluorescence and distinctly surrounded by neuromelanin granules correlated to an ultrastructure of loosely packed and randomly arranged fibrillar material intermixed with dispersed vesicles and clustered mitochondria (Figure 2b and Supplementary Fig 1). This ultrastructural arrangement has previously been attributed to pale bodies[24,25].

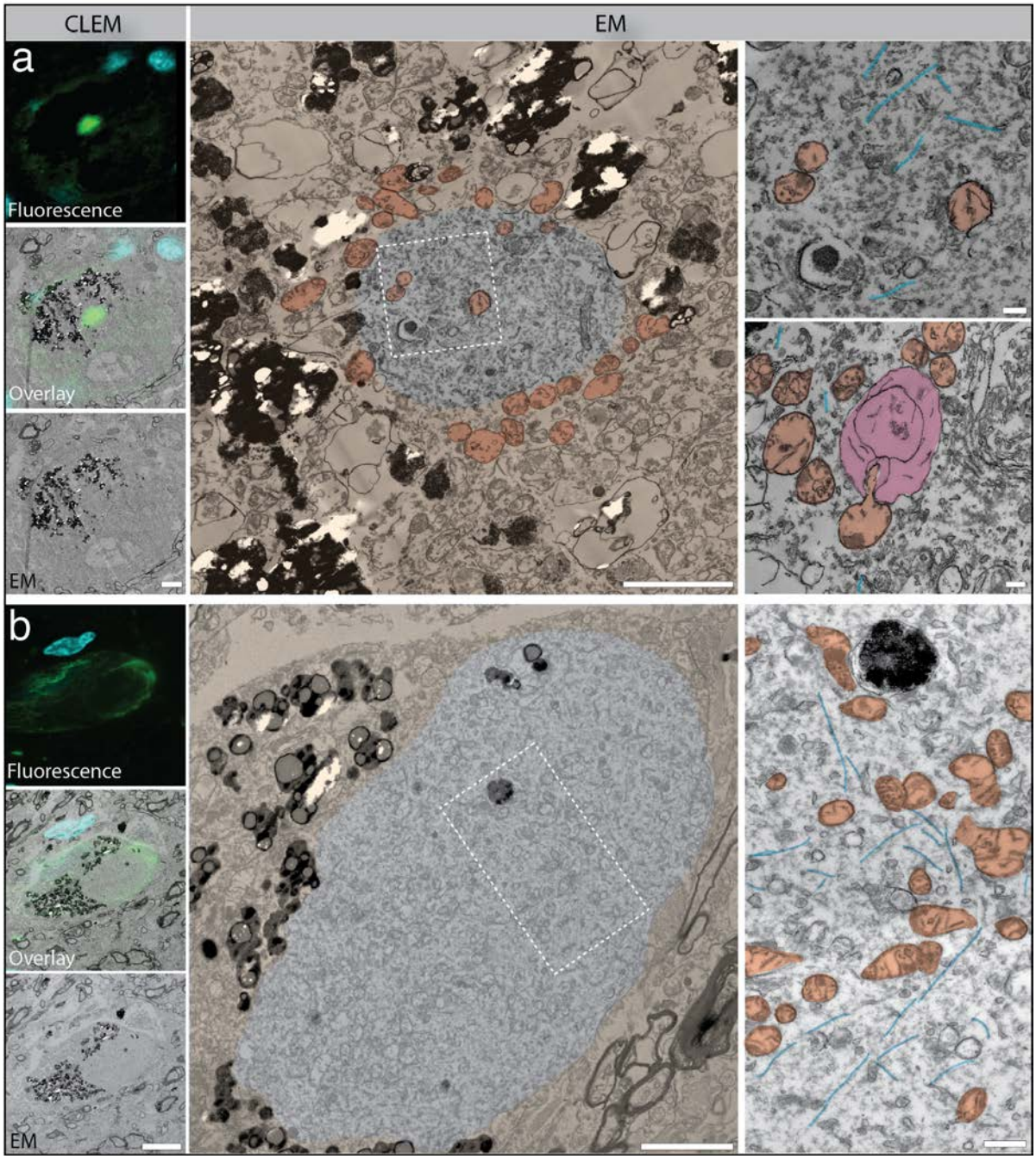

Figure 2: Ultrastructure of small aggregates and pale bodies in neuromelanin cells show dispersed fibrils amongst clustered mitochondria. Inclusions were localized by CLEM^{FL} against aSyn^{pS129} (green; EP1536Y Abcam) and DAPI (cyan). TEM micrographs of a small aggregation center **(a)** and a large aggregate **(b)** reveal the presence of clustered and dysmorphic mitochondria with disrupted cristae (examples coloured in dark orange) interspersed amongst sparse fibrillar material (examples coloured in blue). An autophagosome (pink) ingesting a mitochondria near the small aggregation center was observed. The tissue surrounding the aSyn immuno-positive areas are false-coloured light orange to increase visibility. Scale bars: CLEM - 10 µm; EM - low magnifications - 3 µm, high magnifications - 500 nm

Halo Lewy bodies. Large inclusions showing a distinct peripheral aSyn^{pS129} halo by fluorescence microscopy could be correlated to three distinct fibrillar arrangements by EM with the density of fibril packing assessed by electron tomography and segmentation (Figure 3). The ultrastructures are here classified as: 1-layer inclusions (observed between 3-6 µm diameter), with randomly arranged and loosely packed fibrils (Figure 3a); 2-layer inclusions (observed

between 5-13 μm in diameter), with loosely packed, randomly arranged fibrils at the periphery and a higher density fibrillar mesh at the center (Figure 3b); and 3-layer inclusions (observed between 9-12 μm in diameter), with loosely packed and linear radiating fibrils on the periphery, a higher density fibrillar mesh in the middle, and an electron-dense central core (Figure 3c). The increasing size combined with the increasing level of structural arrangement suggests that these layered ultrastructures represent different stages of LB maturation, starting from a smaller 1-layer LB and ending with the larger 3-layer LB. For all three types, dystrophic mitochondria were consistently observed in the immediate periphery of the fibrillar material, with vesicles of various sizes interspersed amongst the peripheral fibrils. The 2-layer inclusions were observed most frequently, with the 1-layer and 3-layer inclusions being observed comparatively rarely (Supplementary Table 1). Consistent with previous reports[29,34], DAPI staining was seen in the center of the halo LBs (Figure 3c and Supplementary Figure 2). This staining is not attributed to the presence of a cell nucleus in the center of the LB, as the cell nucleus can often be observed in the same or a nearby plane as the LB, but has been hypothesized to be caused by the presence of nucleic acid material[29,34]. Additionally, a clear ring of neurofilament immunostaining was seen surrounding some, but not all, halo LBs (Supplementary Figure 2). However, there was no equally obvious delineation in the ultrastructure between the aSyn fibrils and neurofilament visible in the EM (Figure 3).

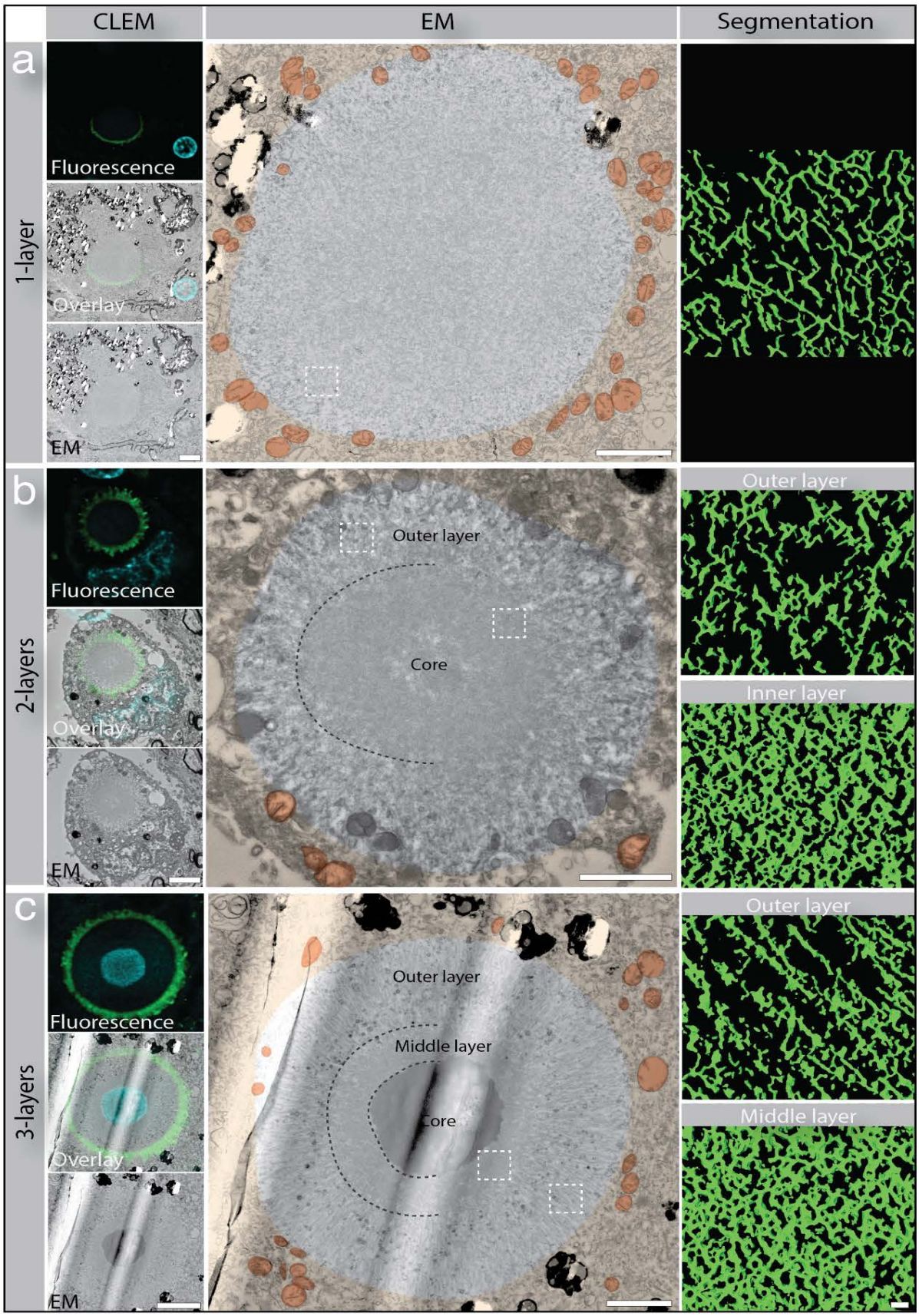

Figure 3: Halo LBs form three distinct ultrastructural arrangements. The inclusions localized within neuromelanin positive neurons by CLEM^{FL} show a halo of aSyn^{pS129} (11a5, Prothena; green). DAPI staining (cyan) is also shown. The EM images show that the fibrils within the halo LBs are arranged into one, two, or three layers, with mitochondria (examples

coloured dark orange) in the periphery of the inclusion. The tissue surrounding the inclusion is false-coloured light orange to increase visibility. The segmentation of electron tomograms taken from within each layer of the LBs (white dotted square) shows the density and orientation of fibril packing. **(a)** In the one-layer LB, the fibrils are homogeneously distributed and randomly arranged across the whole LB. **(b)** In a two-layer LB the outer layer shows a lower density fibril packing compared to the fibrillar mesh that makes up the center. **(c)** The three-layer LB shows a linear arrangement of fibrils in the outer ring, a dense fibrillar mesh in the middle core and a highly electron dense center. A strong DAPI signal was observed in the electron-dense core of the 3-layer LB. The vertical streaks in the EM are due to a tear in the carbon film on the EM grid. Scale bars: CLEM - 4 µm, EM - 2 µm, Segmentation - 50 nm.

In other examples of halo LBs, one had peripheral radiating fibrils and a dense core at its central slice, similar to a 3-layer LB (Figure 4a). However, the core was not as electron dense as for other 3-layer LBs, looking instead to be composed of a dense fibrillar mesh as observed for 2-layer LBs. Additionally, a third layer between the outer peripheral fibrils and dense core was not as clearly defined as for other examples of 3-layer LBs. Therefore, this inclusion appears to be an intermediate between a 2-layer and 3-layer LB supporting the idea that these “layered” ultrastructures represent different stages of halo LB maturation. In a further example of a 3-layer LB, the electron dense core was not spherical, as has always been previously depicted in the literature, but is elongated and irregularly shaped (Figure 4b). With a width measuring 17 µm at its longest point, this inclusion was much larger than the other 3-layer LBs we observed, and therefore could represent two 3-layer LBs merging. Alternatively, it could imply that even at the mature stages, the 3-layer LBs are not solid structures, but are still highly dynamic.

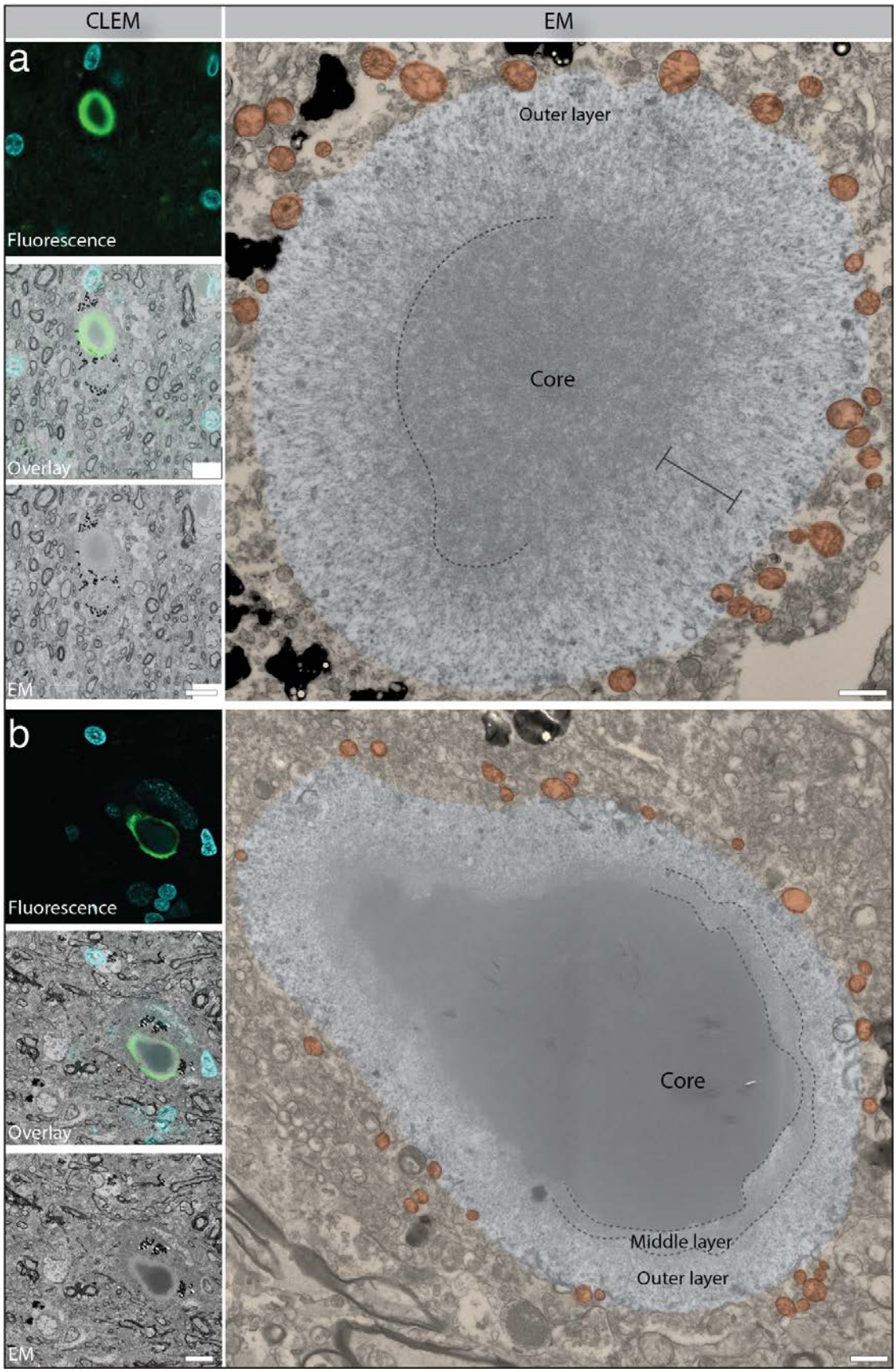

Figure 4: Unconventional halo LB ultrastructures. (a) The EM of this inclusion shows linear radiating fibrils in the outer layer similar to a 3-layer LB. The core is less dense than for a typical 3-layer LB and composed of a fibrillar mesh similar to

a 2-layer LB. There is no clearly defined middle layer, however there is an increased density between the radiating fibrils and dense core (gray bracket), suggesting this inclusion is a transition between a 2-layer and 3-layer LB. **(b)** The electron dense core of this 3-layer LB has an elongated and irregular shape, giving the impression of two 3-layer LBs merging together, or suggests that a 3-layer LB can be highly dynamic. Each inclusion was localized by $CLEM^{FL}$ with the aSyn immunostaining (pS129, EP1536Y Abcam; green) and DAPI staining (cyan) shown. The tissue surrounding the inclusions is false-coloured light orange to increase visibility. Examples of peripheral mitochondria are coloured dark orange. Scale bars: CLEM - 10 µm, high magnification EM - 1µm.

It is important to note that each of the three 'layer' ultrastructures we observed for halo LBs have been previously described in the literature. However, the examples were from different patients, with differences in the (often-long) post-mortem delay, tissue fixation methods and the protocols used for EM preparation. As many of these examples displayed significant ultrastructural extraction in the surrounding tissue ultrastructure, it wasn't clear if the observed ultrastructural differences were due to preparation or post-mortem artifacts[35]. In contrast, our samples have excellent tissue ultrastructural preservation, and we observed examples of each type of halo LB within the same patient (Supplementary Fig 3a), supporting our hypothesis that these "layered" ultrastructures are different stages of halo LB maturation.

When overlaying the fluorescence and EM for the halo LB's, we noted that the pattern of $aSyn^{pS129}$ staining by fluorescence did not correlate with the spatial distribution of total fibrillar material in the LB but was confined to the peripheral edge of the outermost layer of fibrils (Figure 3). It is possible that in free-floating sections, the $aSyn^{pS129}$ antibody may not penetrate the LB center due to the dense packing of fibrils, (particularly in the highly electron-dense core of the 3-layer LB) but that DAPI was able to penetrate the densely packed fibrils as it is a very small molecule compared to an antibody. However, fluorescence microscopy studies have demonstrated a laminar organization of various proteins and aSyn epitopes within LBs[29,36]. To address this, we assessed $aSyn^{pS129}$ IHC staining on ultrathin resin sections where the epitopes are accessible across the entire cross-section of the LB. Here the staining pattern matched more precisely with the ultrastructural fibrillar distribution, however still also showed a pronounced peripheral density for $aSyn^{pS129}$ (Supplementary Figure 3b). In contrast, IHC on adjacent sections with an antibody targeting full-length aSyn showed homogenous staining across the LB. Taken together, these data confirm previous reports that the peripheral $aSyn^{pS129}$ staining represents a specific epitope distribution[29,36].

We also observed examples of neuromelanin containing cells containing multiple halo LBs (Figure 5, Supplementary Figure 4). The halo LBs were either connected by patches of a pale body type ultrastructure of sparse fibrillar material intermixed with clustered mitochondria (Figure 5a,b), or they showed intermixing of the peripheral fibrils at the boundary between the LBs (Figure 5c,d). In some z-planes the boundary between two LBs could not be easily distinguished giving the distinct impression of organizational fluidity (Figure 5c). In one example, we observed a multi-halo LB cell which contained all three types of the layered halo LB ultrastructures (Figure 5d). Taken together, these results support the existing data that pale bodies are precursors to halo LBs and that the different layered halo LB ultrastructures are distinct stages of LB formation.

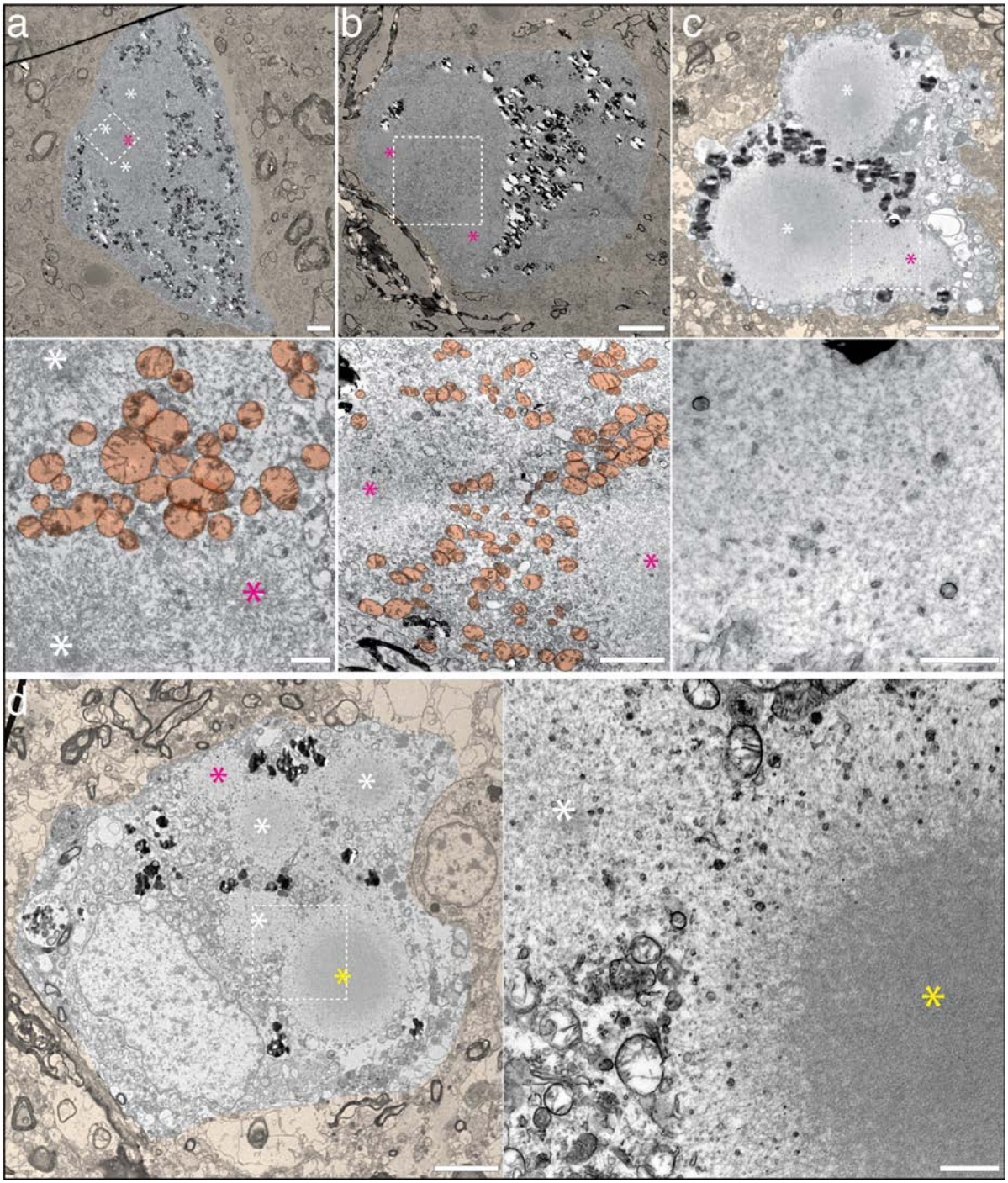

Figure 5: Examples of neurons containing multiple halo LBs. Multiple LBs inside the same neuromelanin containing neuron displaying either the one- (magenta asterisk), two- (white asterisk), or three-layered (yellow asterisk) ultrastructure could be connected by sparse fibrils intermixed with clustered mitochondria (examples coloured orange; a,b) or were directly intermixed at their fibrillar boundaries (c,d). Areas inside white box is shown at higher magnification. The tissue surrounding the cell containing the inclusions is false-coloured light orange to increase visibility. The CLEM localization for these inclusions is shown in Supplementary Figure 4. Scale bars: low magnification - 5 µm; high magnification zooms - 1 µm.

Compact neuritic aSyn pathology displays ultrastructural heterogeneity that is rich in membranes

We next characterized the ultrastructure of large aggregates (>5 µm) that could not be directly associated to neuronal soma as there were no clear cellular demarcations such as an adjacent neuronal cell nucleus, cellular neurofilament staining or neuromelanin in the immediate vicinity of the aggregate (Figure 1e). They were also not classified as bulgy Lewy neurites as their dimensions were not elongated in one dimension (XY, or Z), as would be expected for a Lewy neurite (Figure 1f) but were roughly spherical in 3D. However, as stated previously, the ring of neurofilament staining surrounding the inclusions suggested that they were neuronal in origin and were therefore likely to be compact neuritic inclusions. By EM, we observed ultrastructures for these inclusions rich in densely packed membranous material, as similarly described in our previous study[21] (Figure 6). The spatial distribution of membranes in these inclusions was completely encompassed by the aSyn immunostaining and showed an ultrastructure heavily dominated by vesicular structures and membrane fragments. This composition significantly differed from the mitochondria-rich pale-bodies which only showed sparse vesicles and membrane fragments.

The membranous material could be uniformly distributed and intermixed with accumulated fibrils (Figure 6a). However, in other examples dense fibril accumulations were distinctly surrounded by a halo composed of densely packed membranous material (Figure 6b-e). We additionally identified inclusions that were predominantly fibrillar, with no specific ultrastructural arrangement of the fibrils, and a halo of sparsely distributed membranous material located towards the periphery. (Supplementary Figure 5).

A defining feature of these neuritic inclusions was the presence of a membrane surrounding the aSyn immuno-positive regions (Figure 6, black arrows), ruling out the possibility of them being extracellular LBs[37]. A recent cell model using iPSC-derived dopaminergic neurons described similarly membrane-rich aSyn inclusions that were membrane-bound, and the authors suggested that LBs may therefore form within the lumen of endo/lysosomal organelles[38]. However, in our observations a ring of organized cytoskeleton filaments (likely corresponding to the ring of neurofilament staining observed by immuno-fluorescence (Figure 1f)) could often be observed between the boundary membrane and the aSyn immuno-positive region (Figure 6b,d). Additionally, the membrane could sometimes be observed extending along a projection leading away from the aSyn immuno-positive area (Figure 6e). Therefore, it is likely that this membrane derives from the plasma membrane of the neurite, supporting the idea that these inclusions are compact inclusions within neuritic projections.

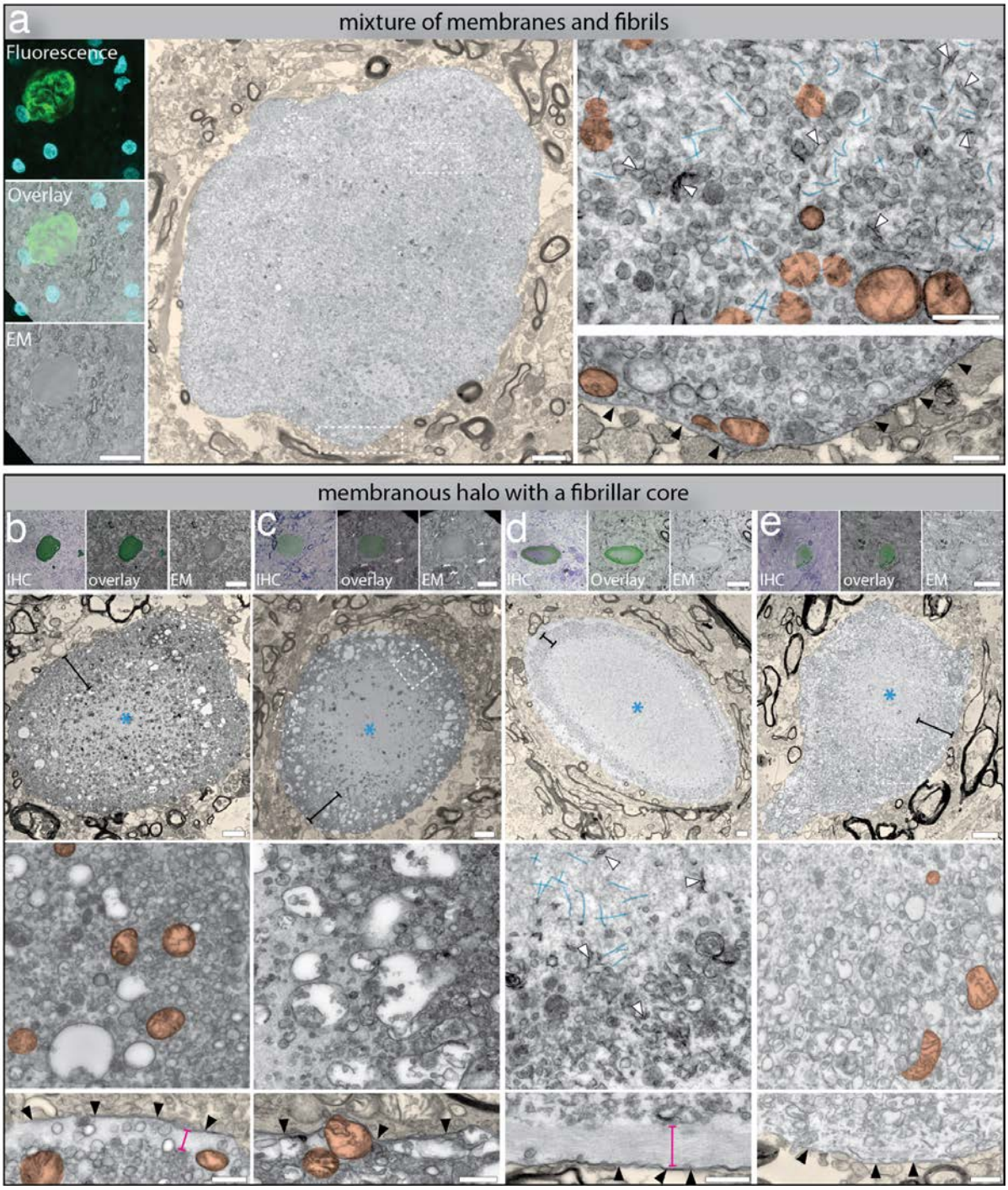

Figure 6. Ultrastructural heterogeneity of compact neuritic pathology. **(a)** An inclusion localized by CLEM^{FL} shows densely packed membranous material intermixed with fibrils. aSyn immunostaining (pS129, EP1536Y Abcam; green) and DAPI (cyan) is shown. **(b-e)** Multiple inclusion showed ultrastructures of a membranous halo (black bracket) surrounding a fibrillar core (blue asterisk). The CLEM^{IHC} shows aSyn immunostaining (b,c,d: LB509, Life Technologies; e: pS129, EP1536Y Abcam; green) overlaid on top of the toluidine blue image from the adjacent slide. The overlay shows the aSyn IHC overlaid with the EM. For all inclusions, the surrounding background tissue has been false-coloured light orange to increase visibility. Examples of mitochondria are coloured in dark orange, fibrils in blue and membrane fragments denoted with white arrowheads. In the higher magnification EM images (white dotted squares), the surrounding neurofilaments (magenta bracket) and neuritic membrane (black arrowheads) are indicated where visible. Scale bars: (a) CLEM - 20µm; low magnification EM - 2 µm, high magnification EM – 500 nm; (b) low magnification EM - 2 µm; high magnification EM - 1 µm; CLEM - 20 µm.

A particular example of note was a compact neuritic inclusion showing multiple discrete puncta composed of various ultrastructural phenotypes within the same aggregate (Figure 7). By EM, this inclusion consisted of a large central aggregate composed of a dense accumulation of membrane fragments, vesicles and mitochondria, where no fibrillar material could be observed (Figure 7a). Two puncta located on the periphery of the large central aggregate were similarly composed only of densely accumulated membranous material, while a third peripheral puncta showed a membranous halo, fibrillar core ultrastructure (Figure 7b). Two of the three small peripheral inclusions are visually distinct from the main central aggregate due to a difference in density of the surrounding membranous material, with the third being visually separated due to a distinct invagination of the main aggregate.

A fourth larger aggregate was composed of a distinctive halo of membrane fragments surrounding a densely packed and disorganized fibrillar core (Figure 7c,d). In the section shown, this fourth aggregate shares no direct intermixing of boundaries with the main inclusion body. However, the two structures are connected by a continuous tract of mitochondria and large vesicles in the surrounding space (Figure 7, black arrows), and show a closer spatial arrangement when observed in adjacent sections (Supplementary Figure 6).

For the main aggregate body, tomography and segmentation additionally did not identify any fibrillar material mixed amongst the densely accumulated membranes (Figure 7a), and neither could any fibrillar material be identified in any of the adjacent sections by EM (Supplementary Figure 6). No nucleus or neuromelanin was observed within the inclusion boundary across the ~20 um for which this inclusion could be followed by EM. Additionally, in one adjacent section, the inclusion appears to be within a projection (Supplementary Figure 6). Therefore, it is likely that this multi-punctum aggregate is also a compact neuritic inclusion.

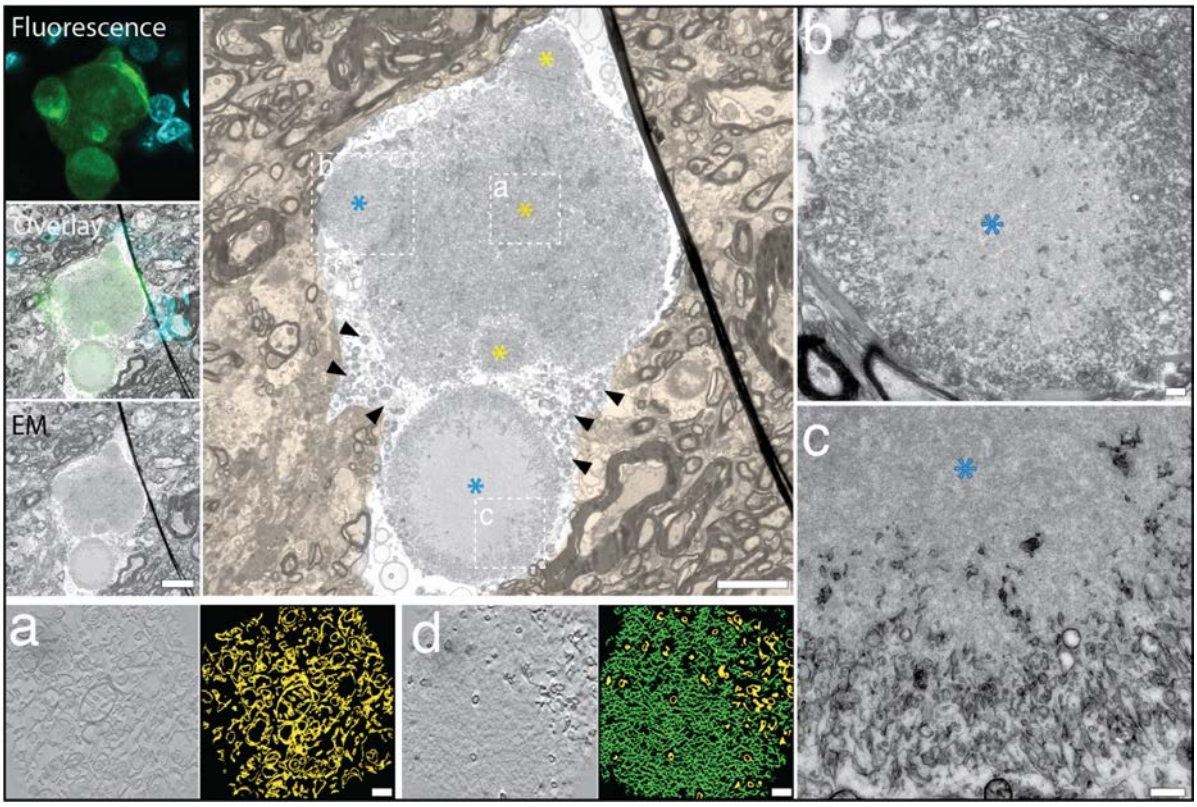

Figure 7. Distinct and multiple ultrastructures within the same neuritic inclusion. An inclusion localized by CLEM^{FL} with aSyn^{pS129} immunostaining (11a5, Prothena; green) and DAPI (cyan) is composed of a main central aggregate and four peripheral puncta. By EM, the main central aggregate plus two peripheral puncta show an ultrastructure of densely packed membranous material (yellow asterisk). The segmentation of an electron tomogram taken from within the central aggregate **(a)** did not reveal the presence of any fibrillar material. The two other peripheral puncta show an ultrastructure of a membranous halo and fibrillar core (blue asterisk) **(b,c)**. The inclusion shown at higher magnification in (b) is taken from an adjacent plane (-1.8 µm) to show the clear membranous halo and fibrillar core. The halo of the larger puncta (c) is composed mainly of membrane fragments. For the z-plane shown, this inclusion is connected to the central aggregate by cellular material such as mitochondria and large vesicles (black arrowheads). The segmentation of an electron tomogram taken from within (c) shows the highly dense packing of the fibrillar core (green) contained within the membranous halo (yellow) **(d)**. Scale bars: CLEM - 10 µm; low magnification EM - 5 µm, high magnification (b,c) - 500 nm; Tomography and segmentation (a,d) - 20 nm.

The distinctive arrangement of the multiple puncta within this single inclusion gives the impression that they have formed at the periphery of the central membranous aggregate and are in a dynamic state of merging with or separating from the larger aggregate. Similar impressions of merging/separating inclusions were seen in other neuritic inclusions (Supplementary Figure 7).

Bulgy Lewy neurites and axonal pathology also shows heterogeneous and membrane-rich ultrastructures

We additionally localized several bulgy Lewy neurites and aSyn immuno-positive axons using CLEM^{IHC} (Figure 8). The bulgy neurites were distinguished by their enlarged, elongated projection through the tissue, where their length was greater than their width (Figure 8 a,b). Axonal pathology was identified by EM from its obvious containment within myelin sheaths (Figure 8 c,d). We found these pathologies also showed the same ultrastructural heterogeneity

as seen for the non-somal inclusions; including, membranes intermixed with fibrils, and the membranous halo, fibrillar core ultrastructure. The membrane-rich ultrastructures were dominated by vesicles and membrane fragments; however, some clustered mitochondria could also be observed. Peripheral cytoskeleton filaments were observed in immuno-negative areas of the axonal inclusions and were easily distinguishable from the aSyn fibrils due to their highly linear and organized spatial arrangement compared to the densely packed (Figure 8c) or disorganized arrangement of the aSyn fibrils (Figure 8d). The neuritic membrane of the bulgy neurite was clearly visible and, for the axonal pathology, cytoskeleton filaments were observed to separate the aSyn immunopositive region from the myelin sheaths. There was no additional membrane specifically containing the aSyn immuno-positive regions for either the bulgy neurites or the axonal pathology, further supporting the idea that the membrane surrounding the compact neuritic aggregates derives from the plasma membrane of the neurite.

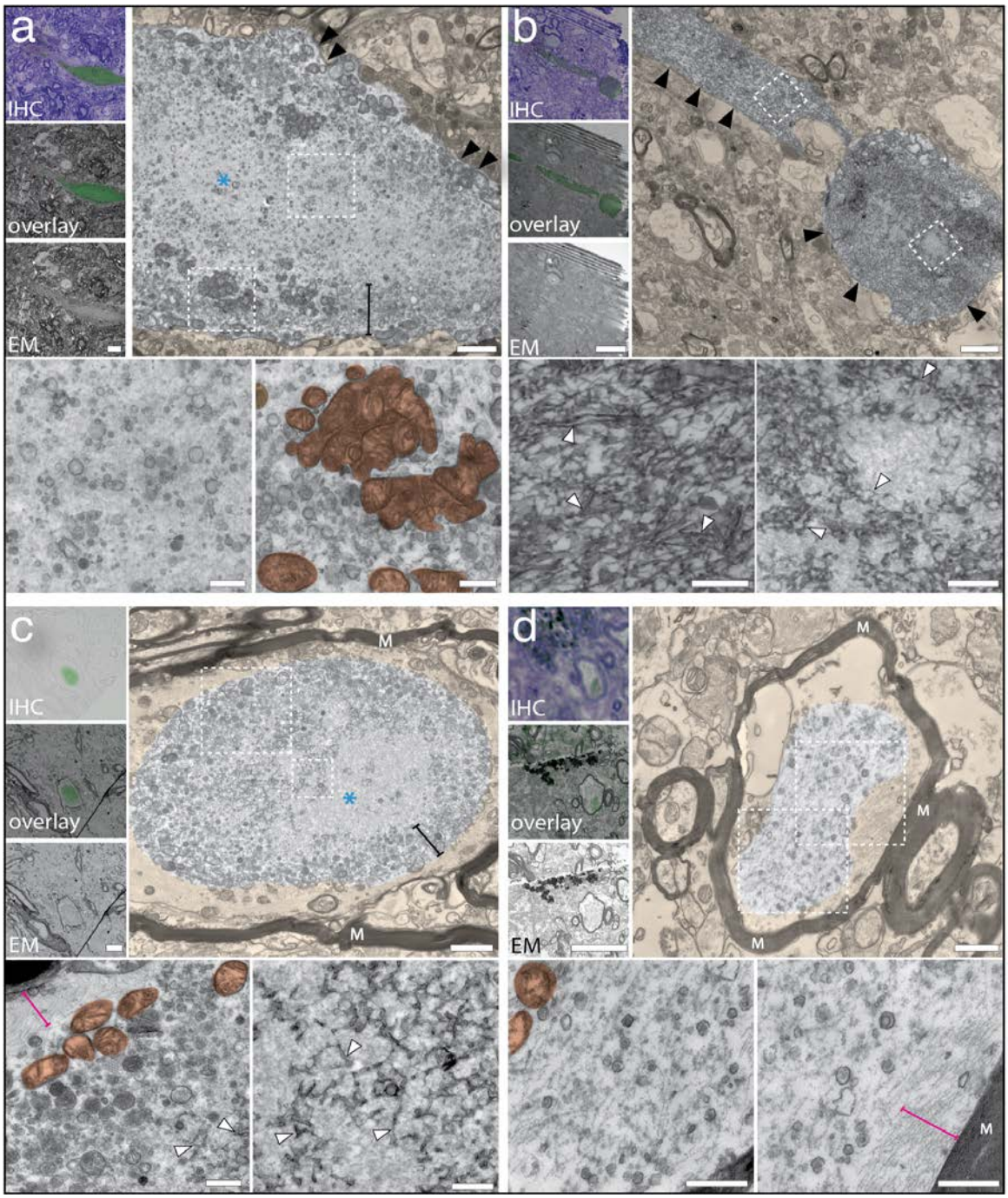

Figure 8. Ultrastructural heterogeneity identified for bulgy Lewy neurites and axonal aSyn pathology. The CLEM^{IHC} localization showing aSyn immunostaining for bulgy Lewy neurites (a,b) and axonal aSyn pathology (c,d) (a,b: LB509, Life Technologies; c: clone42, BD biosciences; d: pS129, EP1536Y Abcam; green) overlaid on top of the toluidine blue image from the adjacent slide. No toluidine blue image was available for panel (c). The overlay panel shows the aSyn IHC overlaid with the EM. The ultrastructure of the bulgy neurite shown in **(a)** has a membranous halo (black bracket) surrounding a fibrillar core (blue asterisk), while **(b)** shows fibrils intermixed with membrane fragments. The axonal aSyn pathology shown in **(c)** has an ultrastructure of a membranous halo (black bracket) composed predominantly of vesicles, with some peripheral mitochondria and some internal patches of accumulated membrane fragments surrounding a fibrillar core (blue asterisk). The axonal pathology shown in **(d)** is composed of aSyn fibrils intermixed with vesicles. For all inclusions the myelin sheath's (M) or neuritic membrane (black arrowheads) are indicated. Areas indicated by white dotted squares are shown at higher magnification. Mitochondria are coloured in orange, membrane fragments are indicated with white arrowheads and cytoskeleton filaments are indicated by a magenta bracket. In all low magnification EM images, the tissue surrounding the aSyn immuno-positive region is false-coloured light orange. Scale bars: CLEM - 10 µm; high mag EM (a,b) - 1 µm, (c,d) - 3 µm; low mag EM - 500 nm.

Discussion

Over the past decades, several efforts have been made to describe the staging of LB formation based on the morphological heterogeneity of aSyn immuno-positive aggregates in human post-mortem brain as seen by IHC staining or immuno-fluorescence[26–29]. In this study, we used CLEM to locate aSyn aggregates in the *substantia nigra* for the various progressive stages, from small punctate cellular staining to the large classical halo LBs. Using this method, we found that aSyn pathology could be categorized by their ultrastructure into two distinct subtypes depending on whether they were contained within the soma of dopaminergic neurons, or not.

Inclusions within the soma of neuromelanin-containing neurons consistently exhibited fibrillar-only ultrastructures, aligning with previous literature associating fibrillar aSyn with mature LBs[6,39] and suggesting a distinct pattern of aSyn aggregation. In this process, initially sparse fibrillar material gradually accumulates together with clustered mitochondria to form large pale bodies. Within the pale bodies the fibrils self-assemble into the three "layered" stages of mature halo LBs, excluding the mitochondria to the periphery of the inclusion. Their increasing size, density of fibril accumulation and the distribution of mitochondria within the somal aSyn inclusions supports an ultrastructural timeline for the formation of fibrillar LBs that follows the previously proposed histological staging of LBs (Figure 9) and is supported by similar observations in seeded cell and mouse models[40,41].

We found that aSyn inclusions not clearly localized within the soma of dopaminergic neurons displayed ultrastructural heterogeneity often dominated by membrane-rich accumulations. We previously determined that aSyn can accumulate together with membranous material in the absence of fibrillar material[21]. Here we now show that the same is true for the phosphorylated form, suggesting that aSyn^{pS129} must be present within these inclusions in a form that is too small to be visible by room-temperature EM, such as aSyn monomers or oligomers. Due to the limited resolution that can be achieved in resin-embedded tissue, the exact structural state of aSyn could not be identified, nor was it possible to determine if aSyn was membrane-bound or intermixed with the membranous material.

The membrane-rich and non-somal inclusions, contained within a surrounding membrane and often a ring of neurofilament, likely represent cross-sections through compact neuritic aSyn aggregates. This hypothesis is supported by our data showing similar membrane-rich ultrastructures in bulgy Lewy neurites and axonal aSyn pathology. Additionally, Forno & Norville described an ultrastructure, similar to what we have now characterized as having a membranous halo and fibrillar core, that were distinguished from classic fibrillar LBs and referred to as "Lewy body-related swellings" found in nerve cell processes[5]. However, it is unclear how the compact neuritic inclusions we observed here relate to the elongated bulgy Lewy neurites. It is possible that the compact neuritic inclusions are precursors to their elongated counterparts, or they could be discrete occurrences. Due to the 60 µm section

thickness limit of our observations, the exact location of these compact neuritic inclusions, with respect to the cell soma or the synapse, remains unclear. However, the often-significant accumulation of vesicles within these compact neuritic aggregates could indicate their proximity to a synapse, or a synaptic origin. A detailed characterization of the membranous components in these inclusions, combined with spatial microscopy studies, could help identify their likely location within the neuron and provide insights into their formation.

Our observation of multiple membranous-type ultrastructures, and their spatial arrangement within a single inclusion (Figure 7), resembles the organization of halo LBs at the periphery of pale bodies. This suggests that different stages of aSyn accumulation can also occur together within neuritic inclusions. Like pale bodies being pre-cursors to halo LBs, in this aggregate, the observation that fibrils were only observed in the peripheral puncta suggests that membrane-only accumulations are a precursor to the formation of the mixed membranous-fibrillar assemblies. Therefore, we propose that the highly membranous environment together with the high local concentration of accumulated aSyn^{pS129} correlates with the presence of a nucleation site for the formation of aSyn fibrils, creating the distinct puncta within the larger aggregate. It has been shown *in vitro* that lipids can stimulate the primary nucleation of aSyn aggregation[42], and many other studies report a modulating effect of lipids on the conformational change and aggregation kinetics of aSyn[43] (and reviewed in[44,45]).

The spontaneous formation of fibrils from within or near the membrane-only inclusions may be driven by phase separation, a phenomenon that has been linked to protein aggregation in neurodegenerative disease, including PD[46–48]. In-vitro studies show aSyn undergoes phase separation before forming amyloid-like states[49–52], lipids can accelerate aSyn phase separation[50], and aSyn affects the phase separation of synaptic vesicles[53]. Additionally, pharmacological interference has been shown to inhibit the primary nucleation and aggregation of aSyn within phase-separated droplets[54].

Further supporting the idea of phase separation, we observed multiple examples where non-somal inclusions were intermixed or had smaller puncta at their periphery, suggesting a dynamic process of aggregate fusion or separation. Such dynamic nature aligns with the behavior of phase-separated droplets in-vitro[55,56]. Furthermore, a recently described aSyn inclusionopathy cell model reported the formation of dynamic, lipid-rich aSyn inclusions that can fuse or dissolve rapidly[57]. These studies, together with our observations in post-mortem human brain, reinforces the notion that the dense membranous aSyn inclusions represent phase-separated droplets that promote the nucleation of aSyn fibrils. Multiple nucleation sites occurring at different time-points could explain the different ultrastructural morphologies observed together within a single inclusion.

However, we also observe evidence of dynamic behavior for the somal inclusions: halo LBs form at the edge of pale bodies, halo LBs which occur together in the same cell were often intermixed at their boundaries and the distinction between them sometimes hard to define, and

our observation of a 3-layer halo LB with a misshapen central electron dense core suggests some fluidity of its three distinct phases. Therefore, these fibrillar structures could also form through a phase-separation event.

For both somal and neuritic inclusions, the initial phase separation of aSyn could be driven by its post-translational modifications and interactions with lipids[50], or other modulators such as salt[58], metal ions[50,51] or ATP[59]. Low levels of ATP have been shown to promote the phase separation of neurodegenerative disease related proteins FUS and amyloid-β[60,61] and mitochondrial dysfunction has been implicated as a disease mechanism for PD. We often observe dystrophic mitochondria in the neuritic inclusions, and they represent a core component of the early stages of fibril accumulation in somal inclusions (e.g. pale bodies). Therefore, a drop in the levels of ATP caused by the breakdown of mitochondria could lead to the phase separation of aSyn and nucleation of fibril formation in either or both the somal or neuritic inclusions. Further studies in the human brain correlating levels of mitochondrial dysfunction in combination with disease staging information could help to further explore this theory.

The distinct spatial separation of the membranous neuritic and fibrillar somal inclusions suggests that they arise through distinct cellular processes. However, how and if the two processes are linked remains unclear. We observe neuritic membranous inclusions without the presence of fibrillar material, which suggests that these inclusions can form spontaneously through the pathological interaction between membranes and aSyn and are the initial sites for aSyn fibrillization. Combined with the current prion-like hypothesis for the formation of somal LBs (reviewed in[62]), it is then plausible that the transmittable aSyn species are produced within these membranous inclusions and spread along the neurite, or between neurons forming the basis of disease pathogenesis. Therefore, based on our current observations in human brain we propose that:

1. non-fibrillar aSyn undergoes phase separation with membranous material in neurites, or at the synapses of affected neurons (membranous-only ultrastructures).
2. nucleation within this environment promotes the spontaneous fibrillization of aSyn (mixture of membranes and fibrils ultrastructures).
3. Accumulated fibrils cluster together, excluding the membranous material to the periphery (membranous halo, fibrillar core ultrastructures).
4. Transmittable fibril species possibly spread along neurites or between neurons via a prion-like mechanism.
5. Fibrils accumulate in the soma together with damaged mitochondria as pale bodies, gradually maturing into classic fibrillar halo LBs (Figure 9).

This hypothesis is supported by recent observations in an iPSC model by Lam et al., showing that seeded aSyn^{pS129} inclusions are distinct from those that form spontaneously (Lam et al., 2022). Furthermore, the idea that membranous neuritic inclusions precede the classic fibrillar

accumulations in the soma of dopaminergic neurons, aligns with existing PD staging information suggesting that pathology starts in the neurites[14]. However, it must be noted that the proposed "toxic" species of aSyn, being oligomers or protofibrils (reviewed in[63]), are too small to be observed by our methods. Therefore, whether the formation of membranous and fibrillar inclusions occur sequentially or independently remains to be verified *in vitro*, and in non-seeding model systems.

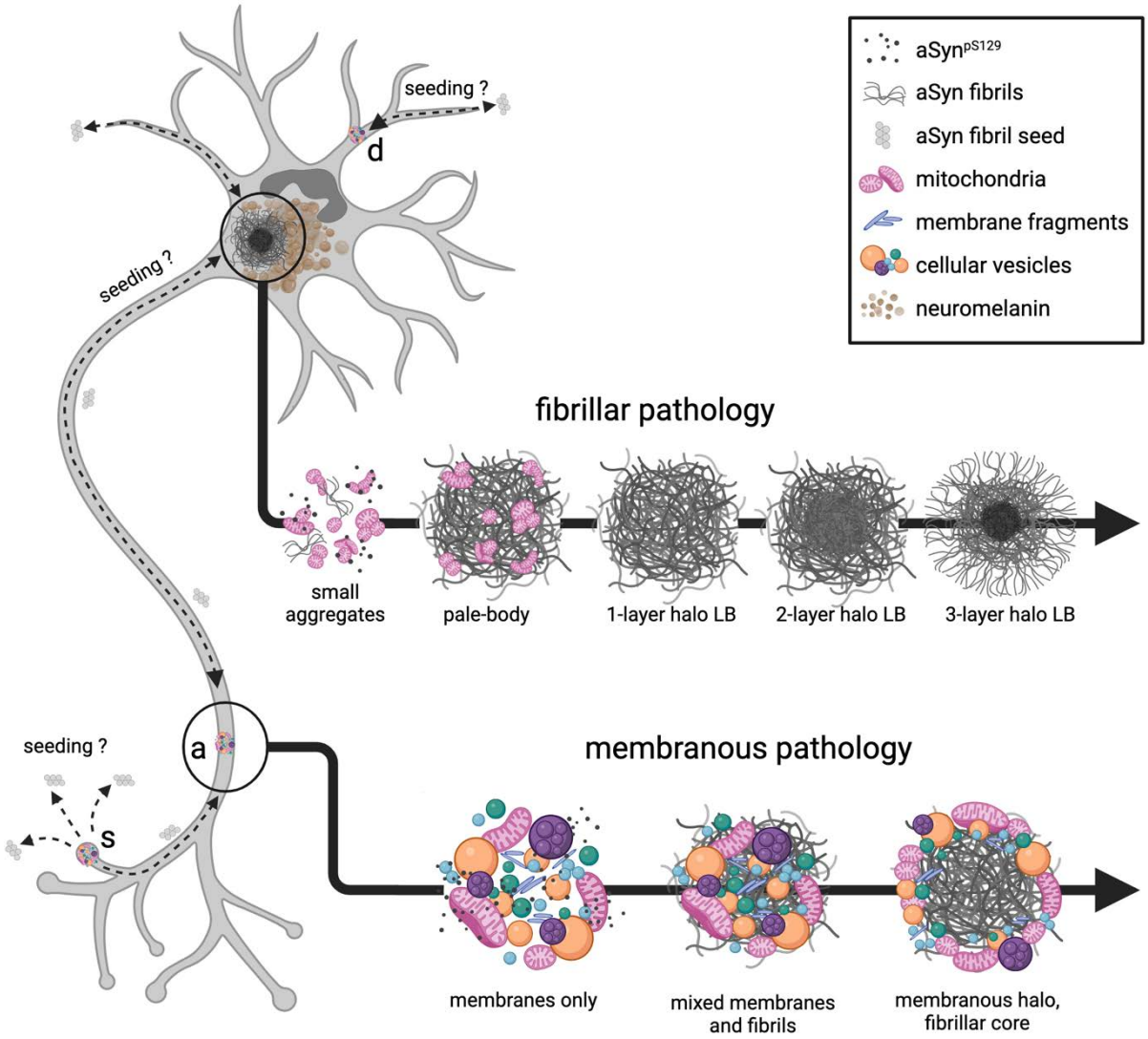

Figure 9. An ultrastructural model for the development of LBs in dopaminergic neurons in the human brain, in which neuritic membranous and somal fibrillar inclusions form via distinct mechanisms. For membranous inclusions, aSyn accumulates together with cellular membranes, vesicles and organelles in the neuritic projections (axons (a), dendrites (d)) and/or at the synapse (s)), providing an environment that nucleates the formation of fibrillar aSyn (membranes only). aSyn fibrils form and accumulate amongst the membranous material (mixed membranes and fibrils) where they cluster together and exclude the membranous material to the periphery of the inclusion (membranous halo, fibrillar core). For fibrillar inclusions, aSyn fibrils accumulate in the soma of dopaminergic neurons together with clustered dystrophic mitochondria to form pale bodies and mature into the layered halo LBs over time. The transmittable aSyn species (oligomers, fibril seeds or mature fibrils) formed within the membranous environments could spread along neurites or between cells via the prion-like mechanism seeding the formation of fibrillar pathology. It is also possible that fibrillar and membranous pathologies occur independently of one another, with the transmittable species from one occurrence seeding the formation of the other.

Our previous finding that the majority of Lewy pathology consists of a crowded membranous environment introduced a lipid-centric hypothesis for the formation of LBs[21] challenging the traditional protein-centric views for PD pathology[6,46,64–66]. Our current data suggests that pathology formation in PD is likely a combination of both; however, the accumulation of damaged membranes may play an important role in promoting the nucleation of aSyn fibril formation. The data presented here bridges numerous studies supporting aSyn and membrane aggregation towards a lipidopathy model of disease pathogenesis with the existing literature on a proteinopathy model for fibrillar LB formation via a prion-like mechanism.

In this study, all inclusions identified by $CLEM^{FL}$ used an antibody against $aSyn^{pS129}$. However, immuno-fluorescence alone could not determine if the ultrastructure of immuno-positive inclusions was fibrillar or membranous. Rather, their location in or outside the soma of neuromelanin containing cells was the main determinant. With numerous microscopy studies reporting differential aSyn epitope staining patterns across synuclein disease pathologies[37,67–71], further CLEM studies are needed to determine whether other markers could better distinguish between fibrillar and membranous aSyn ultrastructures. Additionally, this study focused on full-length aSyn or aSynpS129 immuno-positive inclusions within the substantia nigra of PD patients. While these findings are significant, further research is needed to explore the pathology using different aSyn epitopes, brain regions, and other synuclein diseases to fully understand the broader implications.

Conclusions

Our study marks the first comprehensive ultrastructural exploration capturing the heterogeneous morphological spectrum of Lewy pathology within the *substantia nigra* of PD patients. Our findings delineate membranous and fibrillar $aSyn^{pS129}$ inclusions as discrete entities, suggesting they likely follow distinct aggregation pathways. Specifically, our observations suggest that neuritic membranous aSyn aggregation can nucleate the fibrillization of aSyn, providing the first support from human brain for the spontaneous fibrillization of aSyn leading to disease pathogenesis via the prion-like mechanism. The fibrils could then be transmitted along the neurite, or between neurons, after which they accumulate in the neuronal soma as fibrillar LBs.

Further investigations are now required to understand how and if these two processes are linked. It will also be important to elucidate the initial aggregation mechanism of aSyn with membranous material, identify the cellular identity of the accumulated membranous material and to determine the specific structural state of aSyn in these inclusions.

By mapping the structural diversity of aSyn pathology in the human brain our study provides valuable insights into the process of LB formation in PD and highlights a crucial role for membrane interactions in driving aSyn aggregation. Understanding this pivotal mechanism will be crucial for developing future therapeutic interventions to modify disease onset and progression.

Methods

Human post-mortem brain samples

We included eleven PD brain donors (Donor A-K), who participated in the brain donation program from the Netherlands Brain Bank (www.brainbank.nl) with a post-mortem delay of <7 hrs (Supplementary Table 1). All donors provided written informed consent for a brain autopsy and the use of the material and clinical information for research purposes. Detailed neuropathological and clinical information was made available, in compliance with local ethical and legal guidelines, and all protocols were approved by VU University Medical Center institutional ethics review board (reference number 2019/148). Demographic features and clinical symptoms were abstracted from the clinical files, including sex, age at symptom onset, age at death, disease duration, presence of dementia, core and supportive clinical features for PD.

The brain is dissected at autopsy according to the protocol of the Netherlands Brain bank (https://www.brainbank.nl/brain-tissue/autopsy/). For electron microscopy, the mesencephalon was collected at the level of the oculomotor nerve and subsequently the *substantia nigra* was dissected into 0.5 cm3 tissue blocks at autopsy using a standardized procedure by a neuroanatomist (WvB). These tissue blocks from the *substantia nigra* were immersion fixed in 4 % paraformaldehyde and 0.1 % glutaraldehyde in 0.15 M cacodylate buffer, supplemented with 2 mM calcium chloride, pH 7.4 for 24 hours and stored afterwards in 0.1 paraformaldehyde in 0.15 M cacodylate buffer until further processing for EM

For pathological diagnosis, six or seven µm-thick FFPE-embedded sections were immuno-stained using antibodies against αSyn (clone KM51, 1:500, Monosan Xtra, The Netherlands), amyloid-β (clone 4G8, 1:8000, Biolegend, USA) and phosphorylated tau (p-tau, clone AT8, 1:500, Thermo Fisher Scientific, USA) or processed for Gallyas silver staining, as previously described). Braak αSyn stages were determined using the BrainNet Europe (BNE) staging criteria[26]. Based on Thal phases[72] (amyloid-β), Braak neurofibrillary stages[73] (AT-8 phospho-tau) and CERAD neuritic plaque scores[74] (Gallyas method), levels of AD pathology were determined according to NIA-AA consensus criteria[75]. Additionally, Thal CAA stages[76], presence of aging-related tau astrogliopathy[77] (ARTAG), and microvascular lesions and hippocampal sclerosis were assessed.

CLEM

CLEM was performed as described previously without any modifications[31]. For the fluorescent microscopy, 40-60 µm free-floating brain sections were prepared with a vibratome (Leica VT1200) and immuno-labeled with primary antibodies (aSyn: 11a5 – Prothena - 1/1000, or aSyn^{pS129} EP1536Y - Abcam # 51253 - 1/1000; neurofilament: Sigma Ab5539 - 1/500) overnight at 4 ºC and visualized with Alexa-conjugated secondary antibodies (donkey 488 Molecular Probes A32787 - 1/400, chicken 647 Molecular Probes A32933 - 1/400) and DAPI (Biolegend #422801 - 1/800 dilution) to label cell nuclei after incubation at room-temperature

for 30 mins. 3D fluorescent images were acquired on a confocal TCS SP8 or a Thunder Tissue imager (Leica Microsystems) using a 63 x oil objective (HC PL APO/1.4 numerical aperture). The sections were then resin embedded using a tissue autoprocessor (Leica Microsystems) following the full staining protocol[31]. Trapezoid blocks containing the aSyn pathologies were removed from the resin-embedded section using laser capture microdissection (Leica LMD7) and the resulting blocks glued on the surface of a resin stub. Serial sections of 90 nm (for EM) and 200 nm (for LM) were cut using an ultracut UC7 (Leica Microsystems) and collected consecutively on EM grids and glass slides, respectively. A detailed protocol has been provided in Shafiei et al[31].

Immunohistochemistry was performed on the glass slides. The sections were etched in a saturated potassium ethoxide solution for 3 mins followed by washing in PBS. Endogenous peroxidases were quenched with 1 % hydrogen peroxide in 10 % methanol, before blocking in Dako REAL antibody diluent (Agilent). Antigen retrieval and primary incubations were carried out as outlined in Supplementary Table 3, before washing in PBS supplemented with 0.25 % Triton X and incubation in secondary antibody (ImmPRESS Reagent Anti-Mouse Ig, or Anti-Rabbit Ig, Vector Laboratories) for 30 mins at room temperature. Bound antibody complexes were detected using the permanent HRP Green Kit (Zytomed Systems) with incubation for 3 mins at room temperature. Sections were counterstained with hematoxylin, dehydrated and mounted under glass coverslips for imaging. Adjacent slides were stained with 1% toluidine blue solution. Light microscopy images of selected glass slides containing aSyn immuno-positive structures were collected using a Thunder Tissue imager microscope equipped with a DMI8 color camera (Leica).

TEM images were collected at room temperature on a 120 kV Tecnai G2 Spirit TEM microscope operated at 80 kV with a LaB6 filament and a side mounted EMSIS Veleta camera, a CM100 Biotwin (Philips) operated at 100 kV or a Tecnai Spirit BioTwin (FEI) operated at 80 kV with Lab6 filaments and bottom mounted TVIPS F416 cameras.

Tomography

Tomograms were collected with a pixel size of ~0.5 nm on a Jeol 2100 Plus at 200 kV equipped with a LaB6 filament and TVIPS camera, or a Talos F200C (ThermoFisher Scientific) operating at 200 kV equipped with an X-FEG electron source and a Ceta camera. Exposures of 0.5 seconds were collected every 2 degrees from -60 to +60 degrees. From recorded tilt series, tomograms were reconstructed using IMOD, binned by a factor of 2 and filtered using a non-local means filter in Amira version 2021.2 (ThermoFisher Scientific). Segmentation of the tomograms was carried out using the semi-automated convolutional neural network protocol

of EMAN2 (Tang et al., 2007) and refined using the UCSF Chimera package (Pettersen et al., 2004) and Amira. The final segmentations in the figures show the central 15 slices of the total segmented volume.

Image adjustment

Fluorescent images were deconvoluted using the Leica Thunder algorithm (Leica microsystems, Germany). Brightfield microscopy images were corrected for color-blind readers by replacing the red channel with magenta using FIJI[78]. Both brightfield and EM images were adjusted for brightness and contrast where necessary. EM and fluorescent overlays were created in Adobe Photoshop (2024) using the 'screen' transparency option for the fluorescent image. Toluidine blue/EM and IHC overlays were made in Adobe Illustrator by 'multiplying' the IHC image with the Toluidine blue/EM.

References

1. Lewy, FH. Die Lehre vom Tonus und derBewegung. Zugleich systematische Untersuchungenzur Klinik, Physiologie, Pathologie und Pathogenese der Paralysis agitans. in (Berlin, Springer, 1923).
2. Lewy, FH. Paralysis agitans. Part I: Pathologische Anatomie. in *Handbuch der Neurologie* vol. 3 920–933 (Springer, Berlin, 1912).
3. Spillantini, M. G. *et al.* α-Synuclein in Lewy bodies. *Nature* **388**, 839–840 (1997).
4. Duffy, P. E. & Tennyson, V. M. Phase and electron microscopic observations of Lewy bodies and melanin granules in the Substantia Nigra and Locus Caerulus in Parkinson's disease. *J. Neuropathol. Exp. Neurol.* **24**, 398–414 (1965).
5. Forno, L. S. & Norville, R. L. Ultrastructure of Lewy bodies in the stellate ganglion. *Acta Neuropathol* **34**, 183–197 (1976).
6. Spillantini, M. G., Crowther, R. A., Jakes, R., Hasegawa, M. & Goedert, M. alpha-Synuclein in filamentous inclusions of Lewy bodies from Parkinson's disease and dementia with lewy bodies. *Proc Natl Acad Sci U S A* **95**, 6469–6473 (1998).
7. Wakabayashi, K. *et al.* The Lewy Body in Parkinson's Disease and Related Neurodegenerative Disorders. *Mol Neurobiol* **47**, 495–508 (2013).
8. Desplats, P. *et al.* Inclusion formation and neuronal cell death through neuron-to-neuron transmission of alpha-synuclein. *Proc Natl Acad Sci U S A* **106**, 13010–13015 (2009).
9. Luk, K. C. *et al.* Exogenous alpha-synuclein fibrils seed the formation of Lewy body-like intracellular inclusions in cultured cells. *Proc Natl Acad Sci U S A* **106**, 20051–20056 (2009).
10. Volpicelli-Daley, L. A. *et al.* Exogenous α-synuclein fibrils induce Lewy body pathology leading to synaptic dysfunction and neuron death. *Neuron* **72**, 57–71 (2011).
11. Volpicelli-Daley, L. A., Luk, K. C. & Lee, V. M. Addition of exogenous α-synuclein preformed fibrils to primary neuronal cultures to seed recruitment of endogenous α-synuclein to Lewy body and Lewy neurite–like aggregates. *Nature protocols* **9**, 2135–2146 (2014).

12. Li, J.-Y. *et al.* Lewy bodies in grafted neurons in subjects with Parkinson's disease suggest host-to-graft disease propagation. *Nat Med* **14**, 501–503 (2008).

13. Masuda-Suzukake, M. *et al.* Prion-like spreading of pathological alpha-synuclein in brain. *Brain* vol. 136 1128–38 (2013).

14. Braak, H. *et al.* Staging of brain pathology related to sporadic Parkinson's disease. *Neurobiol Aging* **24**, 197–211 (2003).

15. Fares, M. B., Jagannath, S. & Lashuel, H. A. Reverse engineering Lewy bodies: how far have we come and how far can we go? *Nat Rev Neurosci* **22**, 111–131 (2021).

16. Goedert, M. NEURODEGENERATION. Alzheimer's and Parkinson's diseases: The prion concept in relation to assembled Aβ, tau, and α-synuclein. *Science* **349**, 1255555 (2015).

17. Bisi, N. *et al.* α-Synuclein: An All-Inclusive Trip Around its Structure, Influencing Factors and Applied Techniques. *Front Chem* **9**, 666585 (2021).

18. Fujiwara, H. *et al.* alpha-Synuclein is phosphorylated in synucleinopathy lesions. *Nat Cell Biol* **4**, 160–164 (2002).

19. den Hartog Jager, W. A. Sphingomyelin in Lewy Inclusion Bodies in Parkinson's Disease. *Archives of Neurology* **21**, 615–619 (1969).

20. Gai, W. P. *et al.* In situ and in vitro study of colocalization and segregation of alpha-synuclein, ubiquitin, and lipids in Lewy bodies. *Exp Neurol* **166**, 324–333 (2000).

21. Shahmoradian, S. H. *et al.* Lewy pathology in Parkinson's disease consists of crowded organelles and lipid membranes. *Nature Neuroscience* **22**, 1099–1109 (2019).

22. Leverenz, J. B. *et al.* Proteomic identification of novel proteins in cortical lewy bodies. *Brain Pathol* **17**, 139–145 (2007).

23. Dale, G. E. *et al.* Relationships between Lewy bodies and pale bodies in Parkinson's disease. *Acta Neuropathol* **83**, 525–529 (1992).

24. Hayashida, K., Oyanagi, S., Mizutani, Y. & Yokochi, M. An early cytoplasmic change before Lewy body maturation: an ultrastructural study of the substantia nigra from an autopsy case of juvenile parkinsonism. *Acta Neuropathol* **85**, 445–448 (1993).

25. Gibb, W. R., Scott, T. & Lees, A. J. Neuronal inclusions of Parkinson's disease. *Mov Disord* **6**, 2–11 (1991).

26. Alafuzoff, I. *et al.* Staging/typing of Lewy body related α-synuclein pathology: a study of the BrainNet Europe Consortium. *Acta Neuropathol* **117**, 635–652 (2009).

27. Kuusisto, E., Parkkinen, L. & Alafuzoff, I. Morphogenesis of Lewy Bodies: Dissimilar Incorporation of α-Synuclein, Ubiquitin, and p62. *J Neuropathol Exp Neurol* **62**, 1241–1253 (2003).

28. Wakabayashi, K., Tanji, K., Mori, F. & Takahashi, H. The Lewy body in Parkinson's disease: molecules implicated in the formation and degradation of alpha-synuclein aggregates. *Neuropathology* **27**, 494–506 (2007).

29. Moors, T. E. *et al.* The subcellular arrangement of alpha-synuclein proteoforms in the Parkinson's disease brain as revealed by multicolor STED microscopy. *Acta Neuropathol* **142**, 423–448 (2021).

30. Wakabayashi, K., Mori, F. & Takahashi, H. Progression patterns of neuronal loss and Lewy body pathology in the substantia nigra in Parkinson's disease. *Parkinsonism & Related Disorders* **12**, S92–S98 (2006).

31. Shafiei, N. *et al.* A versatile correlative light and electron microscopy protocol for human brain and other biological models. *bioRxiv* 2024.06.11.598271 (2024) doi:10.1101/2024.06.11.598271.

32. Burtscher, J., Syed, M. M. K., Keller, M. A., Lashuel, H. A. & Millet, G. P. Fatal attraction - The role of hypoxia when alpha-synuclein gets intimate with mitochondria. *Neurobiol Aging* **107**, 128–141 (2021).

33. Nahirney, P. C. & Tremblay, M.-E. Brain Ultrastructure: Putting the Pieces Together. *Front Cell Dev Biol* **9**, 629503 (2021).

34. Power, J. H. T., Barnes, O. L. & Chegini, F. Lewy Bodies and the Mechanisms of Neuronal Cell Death in Parkinson's Disease and Dementia with Lewy Bodies. *Brain Pathol* **27**, 3–12 (2016).

35. Lewis, A. J. *et al.* Imaging of post-mortem human brain tissue using electron and X-ray microscopy. *Current Opinion in Structural Biology* **58**, 138–148 (2019).

36. Prasad, K., Beach, T. G., Hedreen, J. & Richfield, E. K. Critical role of truncated α-synuclein and aggregates in Parkinson's disease and incidental Lewy body disease. *Brain Pathol* **22**, 811–825 (2012).

37. Wiseman, J. A. *et al.* Aggregate-prone brain regions in Parkinson's disease are rich in unique N-terminus α-synuclein conformers with high proteolysis susceptibility. *NPJ Parkinsons Dis* **10**, 1 (2024).

38. Bayati, A. *et al.* A dual hit of α-synuclein internalization and immune challenge leads to the formation and maintenance of Lewy body-like inclusions in human dopaminergic neurons. *bioRxiv* 2023.05.29.542776 (2023) doi:10.1101/2023.05.29.542776.

39. Wakabayashi, K., Matsumoto, K., Takayama, K., Yoshimoto, M. & Takahashi, H. NACP, a presynaptic protein, immunoreactivity in Lewy bodies in Parkinson's disease. *Neurosci Lett* **12;**239(1):45–8, (1997).

40. Mahul-Mellier, A.-L. *et al.* The process of Lewy body formation, rather than simply α-synuclein fibrillization, is one of the major drivers of neurodegeneration. *Proceedings of the National Academy of Sciences* **117**, 4971–4982 (2020).

41. Nuber, S. *et al.* Abrogating Native alpha-Synuclein Tetramers in Mice Causes a L-DOPA-Responsive Motor Syndrome Closely Resembling Parkinson's Disease. *Neuron* vol. 100 75-90 e5 (2018).

42. Galvagnion, C. *et al.* Lipid vesicles trigger α-synuclein aggregation by stimulating primary nucleation. *Nat Chem Biol* **11**, 229–234 (2015).

43. Roeters, S. J. *et al.* Elevated concentrations cause upright alpha-synuclein conformation at lipid interfaces. *Nat Commun* **14**, 5731 (2023).

44. Kiechle, M., Grozdanov, V. & Danzer, K. M. The Role of Lipids in the Initiation of α-Synuclein Misfolding. *Front. Cell Dev. Biol.* **8**, (2020).

45. Ramirez, J., Pancoe, S. X., Rhoades, E. & Petersson, E. J. The Effects of Lipids on α-Synuclein Aggregation In Vitro. *Biomolecules* **13**, 1476 (2023).

46. Moors, T. E. & Milovanovic, D. Defining a Lewy Body: Running Up the Hill of Shifting Definitions and Evolving Concepts. *Journal of Parkinson's Disease* **14**, 17–33 (2024).

47. Mukherjee, S. *et al.* Liquid-liquid Phase Separation of α-Synuclein: A New Mechanistic Insight for α-Synuclein Aggregation Associated with Parkinson's Disease Pathogenesis. *Journal of Molecular Biology* **435**, 167713 (2023).

48. Zbinden, A., Pérez-Berlanga, M., De Rossi, P. & Polymenidou, M. Phase Separation and Neurodegenerative Diseases: A Disturbance in the Force. *Dev Cell* **55**, 45–68 (2020).

49. Hardenberg, M. C. *et al.* Observation of an α-synuclein liquid droplet state and its maturation into Lewy body-like assemblies. *J Mol Cell Biol* **13**, 282–294 (2021).

50. Ray, S. *et al.* α-Synuclein aggregation nucleates through liquid-liquid phase separation. *Nat Chem* **12**, 705–716 (2020).

51. Sawner, A. S. *et al.* Modulating α-Synuclein Liquid–Liquid Phase Separation. *Biochemistry* **60**, 3676–3696 (2021).

52. Ubbiali, D. *et al.* Direct Observation of 'Elongated' Conformational States in α-Synuclein upon Liquid-Liquid Phase Separation. *Angew Chem Int Ed Engl* **61**, e202205726 (2022).

53. Hoffmann, C. *et al.* Synapsin Condensates Recruit alpha-Synuclein. *J Mol Biol* **433**, 166961 (2021).

54. Dada, S. T. *et al.* Pharmacological inhibition of α-synuclein aggregation within liquid condensates. *Nat Commun* **15**, 3835 (2024).

55. Brangwynne, C. P., Mitchison, T. J. & Hyman, A. A. Active liquid-like behavior of nucleoli determines their size and shape in Xenopus laevis oocytes. *Proceedings of the National Academy of Sciences* **108**, 4334–4339 (2011).

56. Molliex, A. *et al.* Phase Separation by Low Complexity Domains Promotes Stress Granule Assembly and Drives Pathological Fibrillization. *Cell* **163**, 123–133 (2015).

57. Lam, I. *et al.* Rapid iPSC inclusionopathy models shed light on formation, consequence and molecular subtype of α-synuclein inclusions. *bioRxiv* 2022.11.08.515615 (2022) doi:10.1101/2022.11.08.515615.

58. Sternke-Hoffmann, R. *et al.* Phase Separation and Aggregation of α-Synuclein Diverge at Different Salt Conditions. *bioRxiv* 2024.03.01.582895 (2024) doi:10.1101/2024.03.01.582895.

59. Rodríguez, L. C., Foressi, N. N. & Celej, M. S. Modulation of α-synuclein phase separation by biomolecules. *Biochim Biophys Acta Proteins Proteom* **1871**, 140885 (2023).

60. Patel, A. *et al.* ATP as a biological hydrotrope. *Science* **356**, 753–756 (2017).

61. Hautke, A. & Ebbinghaus, S. The emerging role of ATP as a cosolute for biomolecular processes. *Biological Chemistry* **404**, 897–908 (2023).

62. Volpicelli-Daley, L. & Brundin, P. Prion-like mechanisms in Parkinson Disease. *Handb Clin Neurol* **153**, 321–335 (2018).

63. Bigi, A., Cascella, R. & Cecchi, C. α-Synuclein oligomers and fibrils: partners in crime in synucleinopathies. *Neural Regen Res* **18**, 2332–2342 (2023).

64. Fanning, S., Selkoe, D. & Dettmer, U. Parkinson's disease: proteinopathy or lipidopathy? *NPJ Parkinsons Dis* **6**, 3 (2020).

65. Lashuel, H. A. Do Lewy bodies contain alpha-synuclein fibrils? and Does it matter? A brief history and critical analysis of recent reports. *Neurobiology of Disease* **141**, 104876 (2020).

66. Lenzi, P. *et al.* Is There a Place for Lewy Bodies before and beyond Alpha-Synuclein Accumulation? Provocative Issues in Need of Solid Explanations. *International Journal of Molecular Sciences* **25**, 3929 (2024).

67. van der Gaag, B. L. *et al.* Distinct tau and alpha-synuclein molecular signatures in Alzheimer's disease with and without Lewy bodies and Parkinson's disease with dementia. *Acta Neuropathol* **147**, 14 (2024).

68. Altay, M. F. *et al.* Development and validation of an expanded antibody toolset that captures alpha-synuclein pathological diversity in Lewy body diseases. *npj Parkinsons Dis.* **9**, 1–21 (2023).

69. Dhillon, J.-K. S. *et al.* A novel panel of α-synuclein antibodies reveal distinctive staining profiles in synucleinopathies. *PLOS ONE* **12**, e0184731 (2017).

70. Kovacs, G. G. *et al.* An antibody with high reactivity for disease-associated α-synuclein reveals extensive brain pathology. *Acta Neuropathol* **124**, 37–50 (2012).

71. Kovacs, G. G. *et al.* Intracellular processing of disease-associated α-synuclein in the human brain suggests prion-like cell-to-cell spread. *Neurobiology of Disease* **69**, 76–92 (2014).

72. Thal, D. R., Rüb, U., Orantes, M. & Braak, H. Phases of A beta-deposition in the human brain and its relevance for the development of AD. *Neurology* **58**, 1791–1800 (2002).

73. Alafuzoff, I. *et al.* Staging of neurofibrillary pathology in Alzheimer's disease: a study of the BrainNet Europe Consortium. *Brain Pathol* **18**, 484–496 (2008).

74. Mirra, S. S. *et al.* The Consortium to Establish a Registry for Alzheimer's Disease (CERAD). Part II. Standardization of the neuropathologic assessment of Alzheimer's disease. *Neurology* **41**, 479–486 (1991).

75. Hyman, B. T. *et al.* National Institute on Aging-Alzheimer's Association guidelines for the neuropathologic assessment of Alzheimer's disease. *Alzheimers Dement* **8**, 1–13 (2012).

76. Thal, D. R., Griffin, W. S. T., de Vos, R. A. I. & Ghebremedhin, E. Cerebral amyloid angiopathy and its relationship to Alzheimer's disease. *Acta Neuropathol* **115**, 599–609 (2008).

77. Kovacs, G. G. *et al.* Aging-related tau astrogliopathy (ARTAG): harmonized evaluation strategy. *Acta Neuropathol* **131**, 87–102 (2016).

78. Schindelin, J. *et al.* Fiji: an open-source platform for biological-image analysis. *Nat Methods* **9**, 676–682 (2012).

Author contributions

AJL, WvdB and HS designed the study. WvdB performed rapid autopsies of PD brain donors and controls, collected brain tissue for EM and performed neuropathological assessment. AJL, LvdH, MDF and DB performed CLEM with assistance from EH and JGJMB for the multi-labelling immuno-fluorescence and fluorescence microscopy. AJL performed the tomography and segmentation. AJL and LvdH prepared the figures and wrote the manuscript. All authors contributed to the analysis and interpretation of the data and final version of the manuscript.

Acknowledgements

We are grateful to the individuals who participated in the brain donation program of the Netherlands Brain bank and their families, making this study possible. We would like to thank Annemieke Rozemuller and the members of the Netherlands Brain Bank autopsy team for facilitating the collection of high-quality post-mortem brain tissue for EM. We thank the staff at the EM Facility at the University of Lausanne and Inayathulla Mohammed from the Laboratory for Biological Electron Microscopy, EPFL for sample preparation and TEM assistance and maintenance, Prothena for providing the pS129 11A5 antibody and the Advanced Optical Microscopy Core O|2 (www.ao2m.amsterdam) for support with confocal imaging. Figure 9 was made using BioRender.com (agreement number BY273AU6CP).

Funding

This work was in part supported by the Swiss National Science Foundation (SNF Grants CRSII5_177195, and 310030_188548), and by the European Union (ERC 4D-BioSTEM, No. 101118656) to HS. Views and opinions expressed are, however, those of the authors only and do not necessarily reflect those of the European Union or the European Research Council Executive Agency. Neither the European Union nor the granting authority can be held responsible for them. AJL was supported by the Synapsis Foundation Switzerland (Grant no. 2019-CDA01), and Parkinson Schweiz. WvdB was supported by the Dutch Parkinson association (Grant no 2020-G01).

Competing Interests

The authors declare no competing interests.

Supplementary Information

Supplementary Table 1. Classification of aSyn inclusions localized by CLEM.

Classification	**Number identified***	**Number of donors**
Somal inclusions		
Small aggregation center	2 (1)	1 (Donor C)
Pale body	12 (3)	5 (Donors A-C,E,H)
1-layer	2 (2)	1 (Donor B)
2-layer	12 (3)	4 (Donors A-C, J)
3-layer	4 (3)	2 (Donors A, B)
Cells containing multiple inclusions	8 (4)	4 (Donors A, B, D, H)
Sub-total somal inclusions	**40 (16)**	**7 different donors**
Compact neuritic inclusions		
Membranous only	3	2 (Donors F, I)
Mixed membranes and fibrils	16 (1)	5 (Donors A, F- I)
Membranous halo, fibrillar core	13 (4)	5 (Donors A, B, E, F, H, I)
Fibrillar	8 (1)	5 (Donors A-C, E, H)
Multiple ultrastructures within one inclusion	5 (4)	1 (Donor A)
Subtotal non-somal inclusions	**45 (10)**	**6 different donors**
Bulgy neurite/axonal inclusions		
Bulgy neurite	4 (2)	4 (Donors A, B, F, H)
Axonal	3 (2)	1 (Donor B)
Sub-total	**7 (4)**	**4 different donors**
Total	**92**	**10**

*These numbers are not an indication of the total prevalence of each type of inclusion within the *substantia nigra*. Brackets () indicate the number of inclusions shown in this manuscript.

Supplementary Table 2. Demographic details and neuropathological features of the included PD brain donors used for this study.

ID donor	Diagnosis		age at death (y)	F/M	PMD (h:m)	Brain weight (g)	ABC	Braak aSyn stage	Braak NFT stage	Thal Phase	CAA	Other
	Clin.	Path.										
A	PD	PD	71	M	5:55	1215	A1B0C0	6	1	1	0	–
B	PDD	PDD	88	M	4:05	1405	A2B2C2	6	3	3	2	Infarction in hippocampus
C	PDD	PDD	85	M	6:50	1200	A1B1C0	6	2	0	0	LATE 1 out of 3; ARTAG
D	PD	PD	83	M	6.25	1387	A1B2C0	6	3	1	0	ARTAG
E	PD	PD	87	F	6:20	1290	A1B2C0	6	3	1	0	PART 3 out of 6; ARTAG
F	PD	PD	63	M	5:55	n.d.	0	5	2	0	0	–
G	PD	PDD	90	F	4:45	1335	B	6	3	3	2	–
H	PD	PDD	74	M	5:15	1350	0	6	2	3	1	–
I	PD	PD	84	M	4:50	1430	0	5	3	0	0	–
J	PD	PD	87	M	6:10	1244	A2B2C1	6	2	3	2	–

Clin. =clinical diagnosis; Path. =pathological diagnosis; y= year; F/M=female/male; PMD= postmortem delay; h=hours; m=minutes; g=grams; ABC = ABC criteria according to Montine et al.[1] Braak aSyn stage[2], NFT= neurofibrillary tangle, Braak NFT stage[3], Thal Phase[4], CAA[5], ARTAG[6], n.d.= no data. Representative images from donors A-G are shown in this study.

Supplementary Table 3. Immunohistochemistry conditions for primary antibodies.

Antibody	Antibody target	Company information	Dilution from stock	Incubation conditions	Antigen retrieval conditions
LB509	aSyn	Life Technologies (# 180215)	1/500	1 hour, 37 °C	None
Clone 42	aSyn	BD Biosciences (# 15895639)	1/100	4 hours, room temperature	100% formic acid 10 mins, Tris-EDTA pH 9 at 100 °C for 30 mins
EP1536Y	$aSyn^{pS129}$	Abcam (# 51253)	1/1000	overnight, 4 °C	None
11a5	$aSyn^{pS129}$	Prothena (gift)	1/100,000	1 hour, 37 °C	None

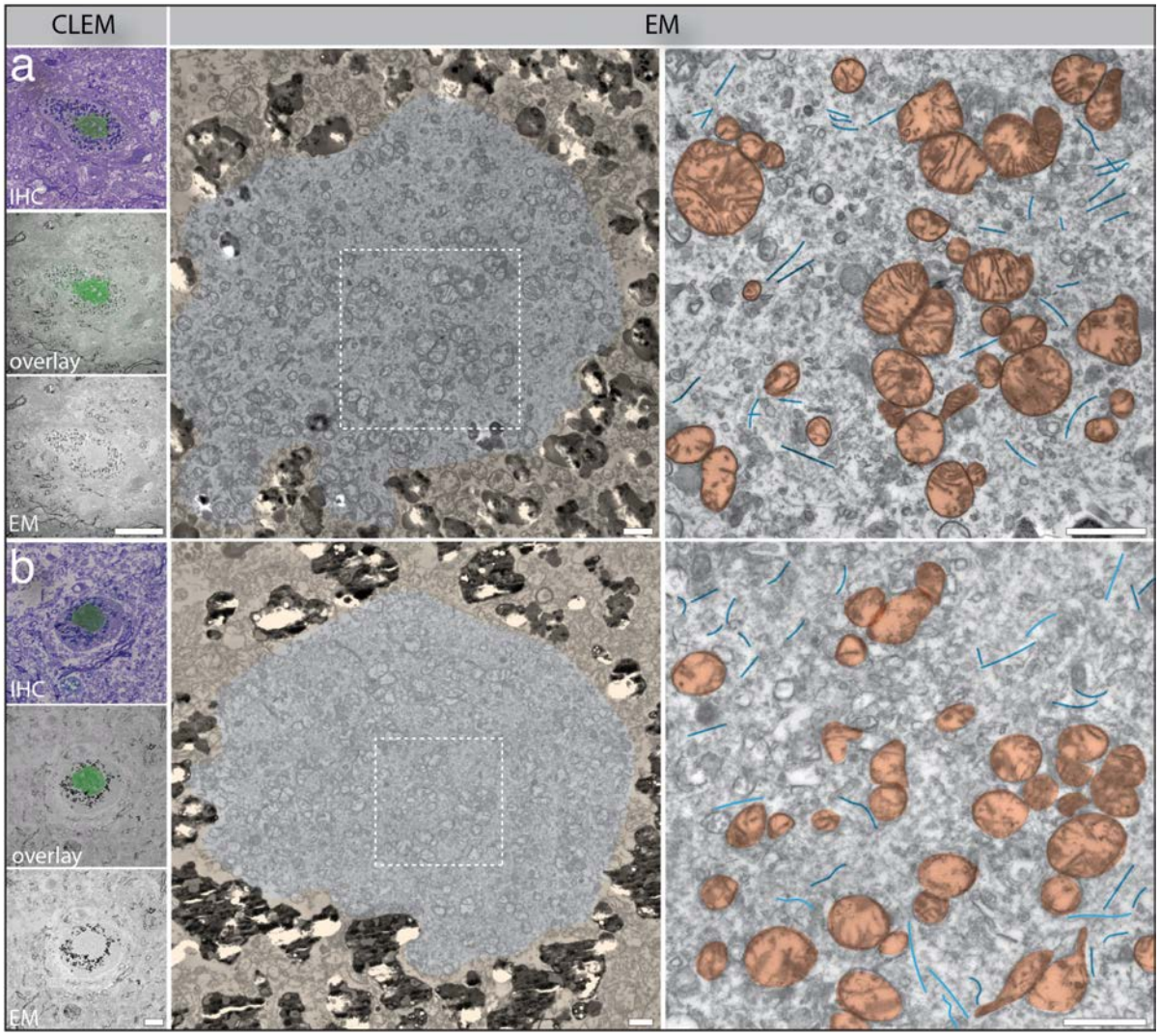

Supplementary Figure 1. Further examples of pale bodies. Large aggregates in neuromelanin containing neurons localized by CLEM^{IHC} show immuno-staining of aSyn (a - clone 42, BD Biosciences; b - 11a5, Prothena; green) overlaid on top of the toluidine blue image from the adjacent slide. The overlay panel shows the aSyn IHC overlaid with the EM. The EM shows an ultrastructural arrangement of accumulated and clustered mitochondria (examples coloured in dark orange) interspersed amongst fibrillar material (examples coloured in blue). The tissue surrounding the aSyn immuno-positive areas are false-coloured light orange to increase visibility. Scale bars: CLEM (a) - 5 µm, CLEM (b) - 10 µm; EM in center and right panels - 1 µm.

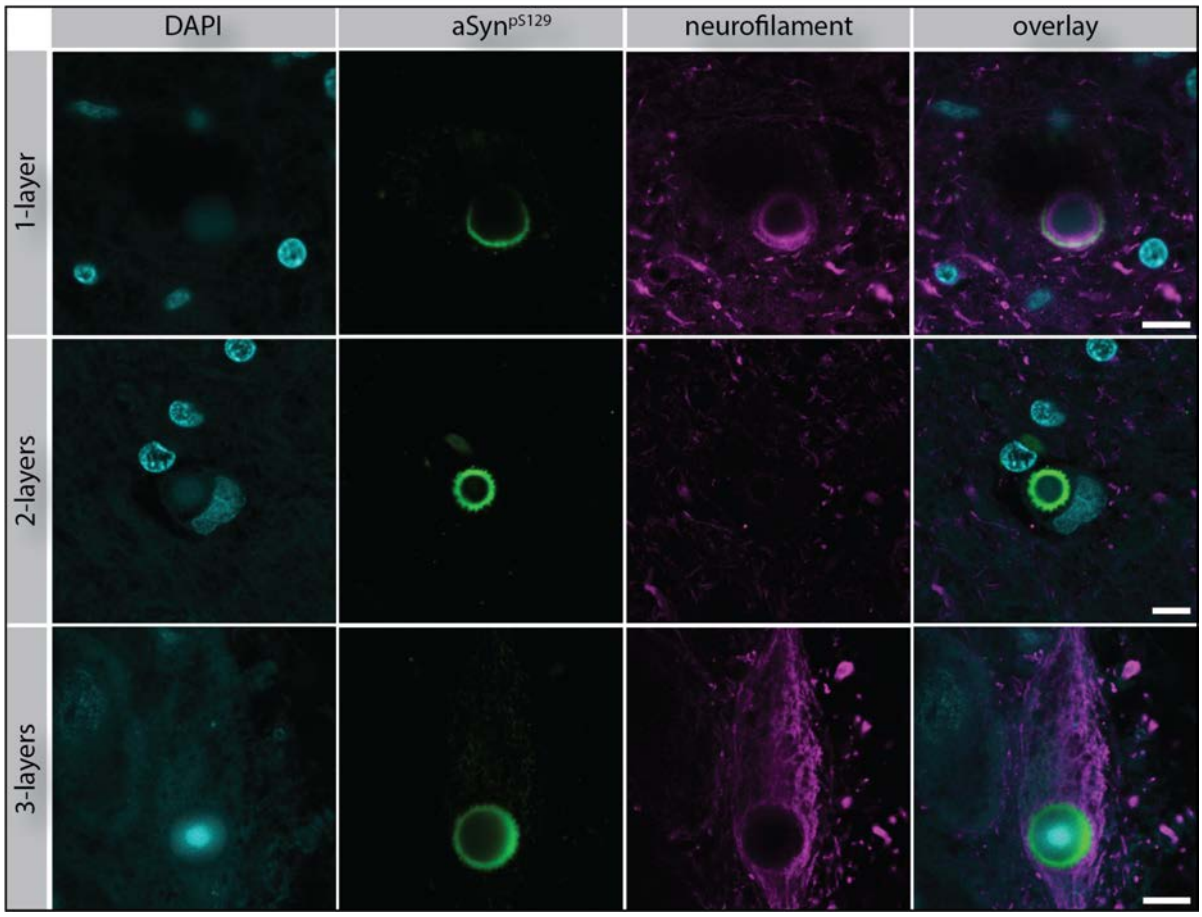

Supplementary Figure 2: Neurofilament staining in Halo LBs. Raw fluorescent images taken from the central plane of the halo LBs shown in Figure 3. Immunostaining against cell nuclei (DAPI; cyan), aSyn^{pS129}(11a5, Prothena; green), and neurofilament (neurofilament H, Sigma; magenta) is shown. A double neurofilament ring surrounding the aSyn^{pS129} halo is observed for the one-layer LB, a very faint neurofilament ring was observed for the two-layer LB, and the three-layer LB shows cellular neurofilament staining concentrated around the periphery of the LB. Panels in each row show the same field of view. Scale bars: 10 µm.

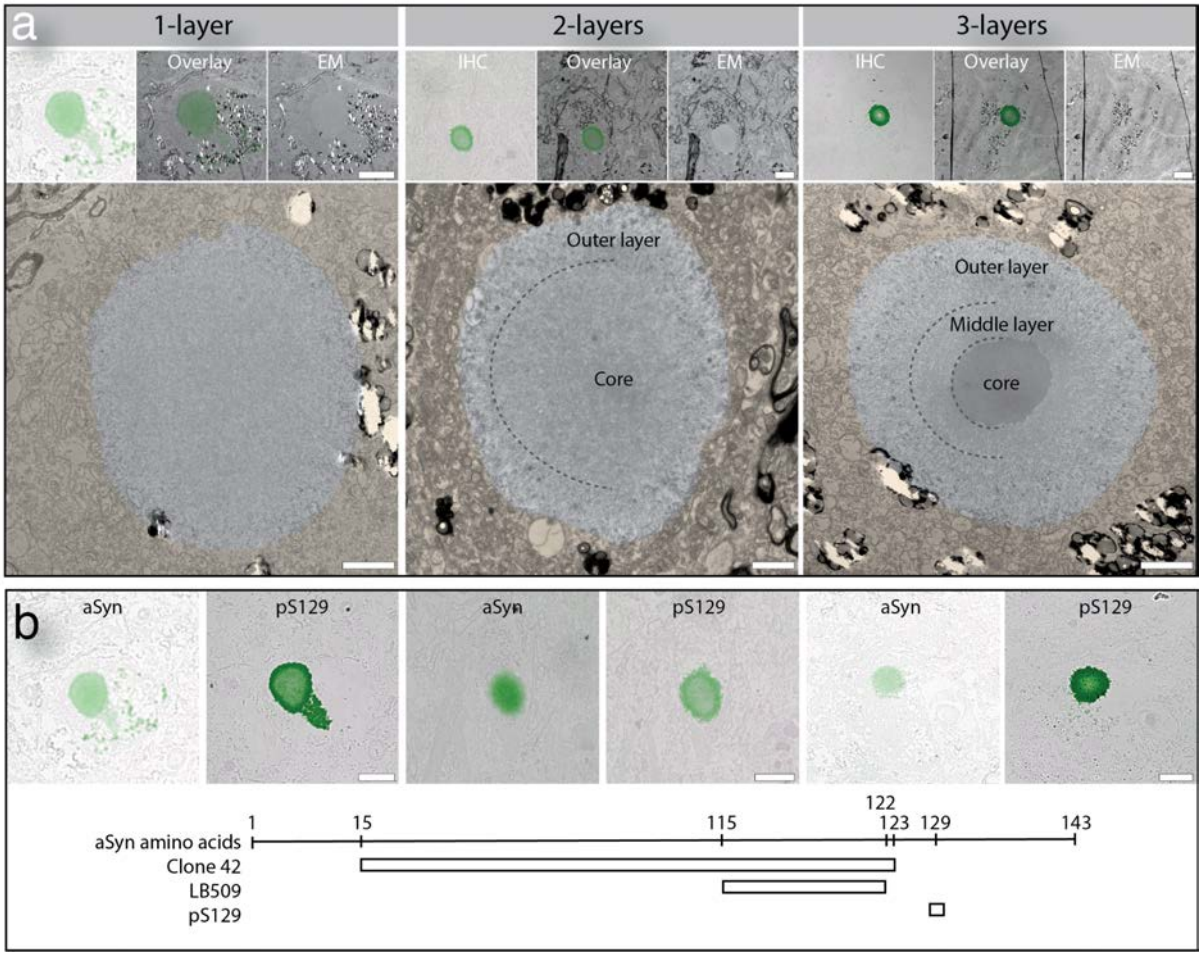

Supplementary Figure 3: Halo LBs localized within the same brain donor. (a) Examples of the one-, two- and three-layer halo LBs localized by CLEM^{IHC} within the *substantia nigra* of donor B. aSyn immuno-positive staining (one- and two- layer LBs: Clone 42, BD Biosciences; three-layer LB: LB509, Life Technologies; green) is shown for the IHC. The tissue surrounding the inclusion is false-coloured orange. **(b)** Adjacent ultrathin sections for the LBs shown in (a) were immunostained with aSyn (clone 42, BD Biosciences) or aSyn^{pS129} (EP1536Y, Abcam). The amino acid epitopes of aSyn recognized by each antibody used are shown. Scale bars: top panels in (a) - 10 µm; bottom panels in (a) - 2 µm; (b) - 10 µm.

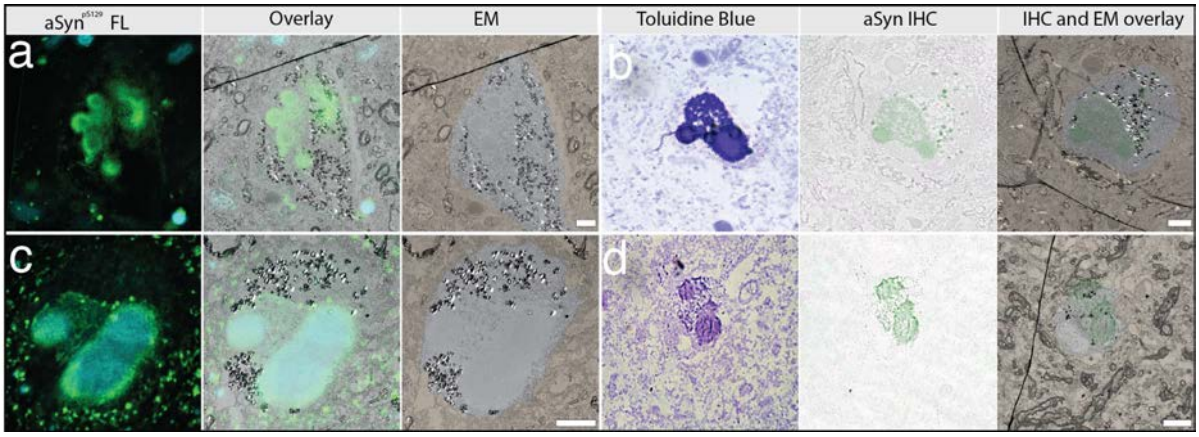

Supplementary Figure 4: CLEM localization of multi- halo LB neurons. aSyn immuno-positive staining (green**)** as seen by fluorescence (aSyn^{pS129} a: EP1536Y, Abcam; c - 11a5, Prothena) or IHC (b, d - clone 42, BD Biosciences) for inclusions shown in Figure 5. DAPI staining (cyan) is also shown for the CLEM^{FL}. Sections adjacent to the IHC were stained with toluidine blue to assist with the correlation between the IHC and the EM. The correlation for the inclusion shown in (c) was performed on an adjacent grid to that shown in Figure 5c. The tissue surrounding the cell containing the inclusions is false-coloured light orange to increase visibility. Scale bars: 7 µm.

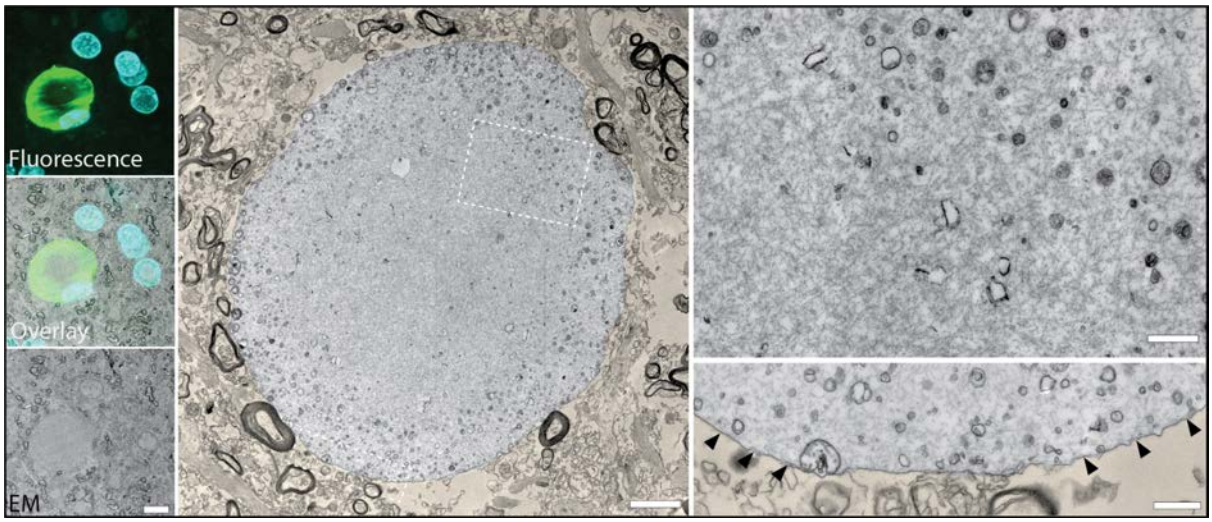

Supplementary Figure 5: Neuritic pathology can also be predominantly fibrillar. The CLEM^{FL} shows aSyn^{pS129} (EP1536Y Abcam; green) and DAPI (cyan) immunostaining. EM images show the inclusion is predominantly fibrillar with a halo of sparse membranous material at the periphery. The background tissue has been false-coloured light orange to increase visibility. The neuritic membrane surrounding the inclusion is indicated with black arrowheads in the higher magnification images (white dotted squares). Scale bars: low mag EM- 2 µm, high mag EM -500 nm.

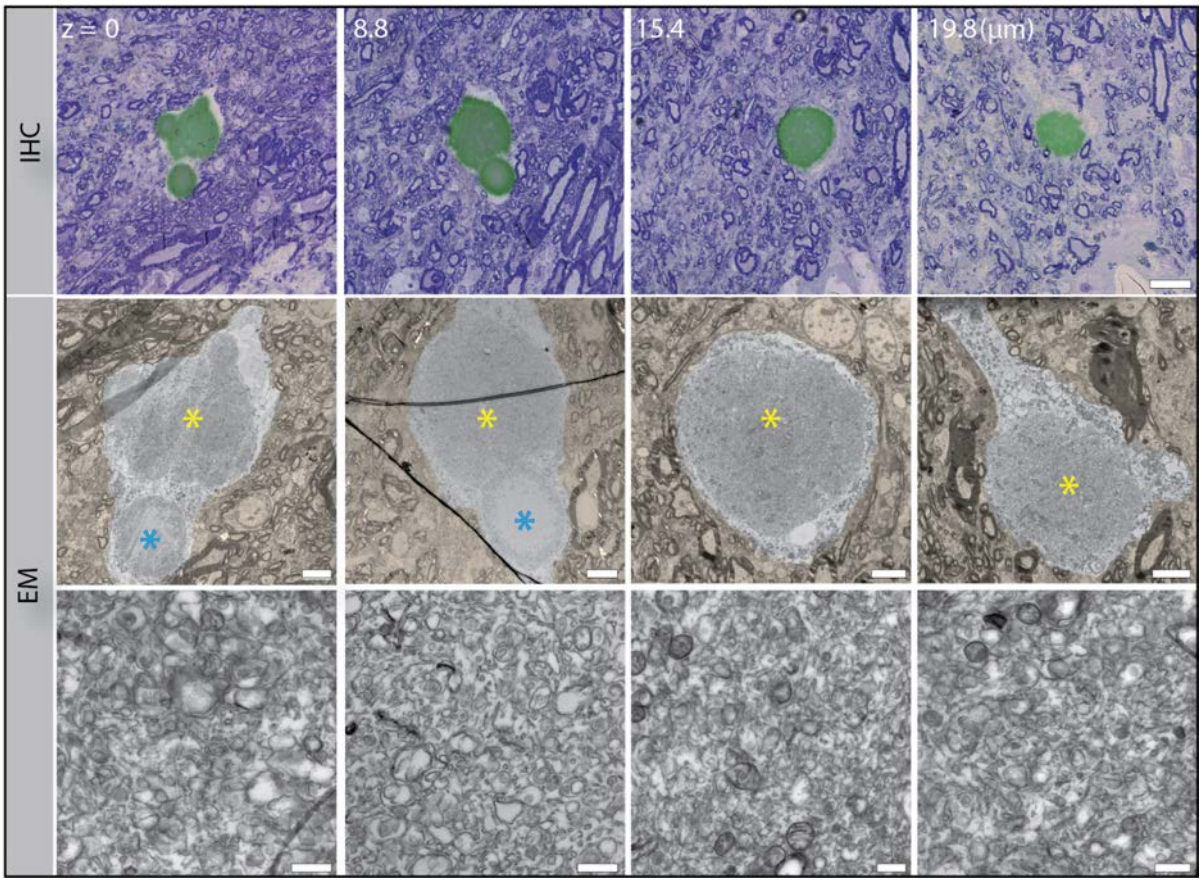

Supplementary Figure 6. **Distinct and multiple ultrastructures within the same neuritic inclusion.** The same inclusion shown in Figure 7 is shown through ~ 20 um of tissue along the z-axis. aSyn immunostaining (LB509; green) overlaid on top of the toluidine blue image from the adjacent slide is shown for each corresponding EM image. Higher magnification EM images taken from within the main central aggregate all the way through the inclusion shows the same ultrastructure of densely accumulated membranous material, with no evidence of fibrils. The inclusion at z =19.8 µm looks to be in a neuritic projection. For all low magnification images, the tissue surrounding the aSyn immuno-positive region is false-coloured light orange to increase visibility. The inclusion at z =19.8 µm looks to be in a neuritic projection. Scale bars: low magnification EM - 5 µm, high magnification EM - 500 nm; IHC - 20 µm.

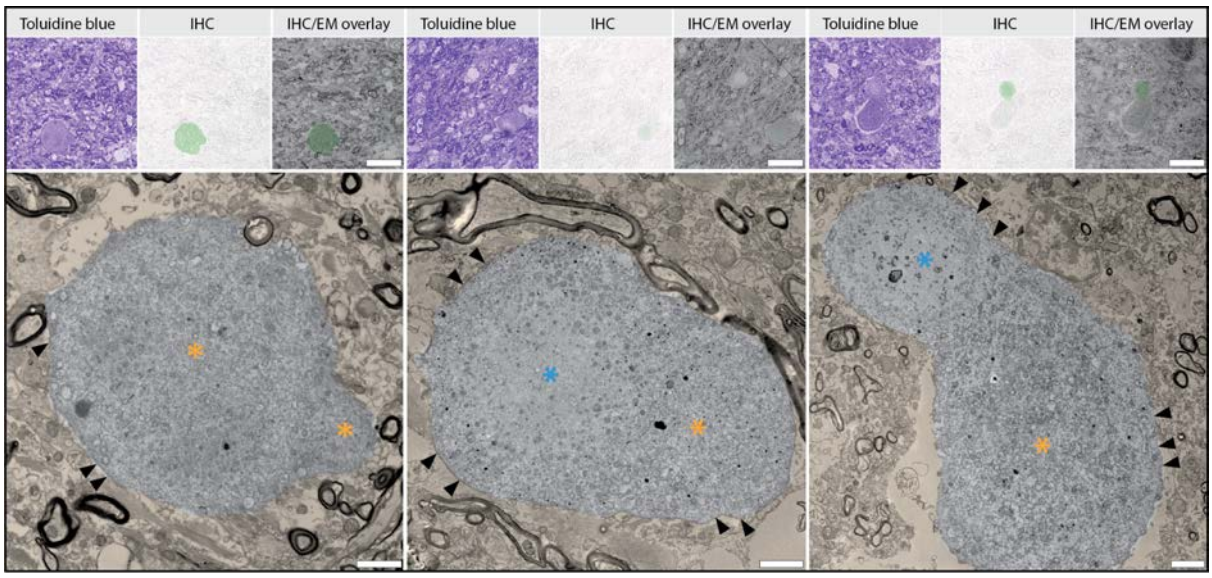

Supplementary Figure 7: Further examples of merging/separating neuritic aSyn inclusions. Multiple ultrastructures were observed within the inclusions including intermixed fibrils and membranes (orange asterisk) or a membranous halo, fibrillar core (blue asterisk). The CLEM^{IHC} shows aSyn immuno-positive staining (green; clone 42, BD Biosciences). The toluidine blue image from the adjacent slide is also shown. The tissue surrounding the aSyn immuno-positive region is false-coloured light orange to increase visibility. The neuritic membrane surrounding the inclusions are indicated with black arrowheads. Scale bars: 2 µm.

Supplementary References

1. Montine, T. J. *et al.* National Institute on Aging-Alzheimer's Association guidelines for the neuropathologic assessment of Alzheimer's disease: a practical approach. *Acta Neuropathol* **123**, 1–11 (2012).
2. Alafuzoff, I. *et al.* Staging/typing of Lewy body related α-synuclein pathology: a study of the BrainNet Europe Consortium. *Acta Neuropathol* **117**, 635–652 (2009).
3. Alafuzoff, I. *et al.* Staging of neurofibrillary pathology in Alzheimer's disease: a study of the BrainNet Europe Consortium. *Brain Pathol* **18**, 484–496 (2008).
4. Thal, D. R., Rüb, U., Orantes, M. & Braak, H. Phases of A beta-deposition in the human brain and its relevance for the development of AD. *Neurology* **58**, 1791–1800 (2002).
5. Thal, D. R., Griffin, W. S. T., de Vos, R. A. I. & Ghebremedhin, E. Cerebral amyloid angiopathy and its relationship to Alzheimer's disease. *Acta Neuropathol* **115**, 599–609 (2008).
6. Kovacs, G. G. *et al.* Aging-related tau astrogliopathy (ARTAG): harmonized evaluation strategy. *Acta Neuropathol* **131**, 87–102 (2016).